

	<p>VYSOKÉ UČENÍ TECHNICKÉ V BRNĚ BRNO UNIVERSITY OF TECHNOLOGY</p>
	<p>FAKULTA ELEKTROTECHNIKY A KOMUNIKAČNÍCH TECHNOLOGIÍ ÚSTAV RADIOELEKTRONIKY</p> <p>FACULTY OF ELECTRICAL ENGINEERING AND COMMUNICATION DEPARTMENT OF RADIO ELECTRONICS</p>

IMPLEMENTATION AND TEST OF A 2D-INTEGRAL EQUATION MoM-ALGORITHM FOR THE ANALYSIS OF POWER-BUS STRUCTURES ON PRINTED CIRCUIT BOARDS

IMPLEMENTACE A OVĚŘENÍ ALGORITMU ZALOŽENÉM NA ŘEŠENÍ 2D INTEGRÁLNÍ
ROVNICE PRO ANALÝZU POWER-BUS STRUKTUR DESEK PLOŠNÝCH SPOJŮ

DIPLOMOVÁ PRÁCE
MASTER'S THESIS

AUTOR PRÁCE
AUTHOR

Bc. Martin Štumpf

VEDOUCÍ PRÁCE
SUPERVISOR

prof. Dr.-Ing. Marco Leone

LICENČNÍ SMLOUVA POSKYTOVANÁ K VÝKONU PRÁVA UŽÍT ŠKOLNÍ DÍLO

uzavřená mezi smluvními stranami:

1. Pan/paní

Jméno a příjmení: Bc. Martin Štumpf
Bytem: Lipoltice 88, Lipoltice, 533 64
Narozen/a (datum a místo): 22. září 1983 v Čáslavi

(dále jen „autor“)

a

2. Vysoké učení technické v Brně

Fakulta elektrotechniky a komunikačních technologií
se sídlem Údolní 53, Brno, 602 00
jejímž jménem jedná na základě písemného pověření děkanem fakulty:
prof. Dr. Ing. Zbyněk Raida, předseda rady oboru Elektronika a sdělovací technika
(dále jen „nabyvatel“)

Čl. 1

Specifikace školního díla

1. Předmětem této smlouvy je vysokoškolská kvalifikační práce (VŠKP):

- ☐ disertační práce
 - ☒ diplomová práce
 - ☐ bakalářská práce
 - ☐ jiná práce, jejíž druh je specifikován jako
- (dále jen VŠKP nebo dílo)

Název VŠKP: Implementation and Test of a 2D Integral Equation MoM-Algorithm for the Analysis of Power-Bus Structures on Printed Circuit Boards

Vedoucí/ školitel VŠKP: prof. Dr.-Ing. Marco Leone

Ústav: Institute for Fundamental Electrical Engineering and Electromagnetic Compatibility

Datum obhajoby VŠKP: _____

VŠKP odevzdal autor nabyvateli*:

- ☒ v tištěné formě – počet exemplářů: 2
- ☒ v elektronické formě – počet exemplářů: 2

2. Autor prohlašuje, že vytvořil samostatnou vlastní tvůrčí činností dílo shora popsané a specifikované. Autor dále prohlašuje, že při zpracovávání díla se sám nedostal do rozporu s autorským zákonem a předpisy souvisejícími a že je dílo dílem původním.

3. Dílo je chráněno jako dílo dle autorského zákona v platném znění.

* hodící se zaškrtněte

4. Autor potvrzuje, že listinná a elektronická verze díla je identická.

Článek 2

Udělení licenčního oprávnění

1. Autor touto smlouvou poskytuje nabyvateli oprávnění (licenci) k výkonu práva uvedené dílo nevýdělečně užít, archivovat a zpřístupnit ke studijním, výukovým a výzkumným účelům včetně pořizování výpisů, opisů a rozmnoženin.
2. Licence je poskytována celosvětově, pro celou dobu trvání autorských a majetkových práv k dílu.
3. Autor souhlasí se zveřejněním díla v databázi přístupné v mezinárodní síti
 - ☒ ihned po uzavření této smlouvy
 - ☐ 1 rok po uzavření této smlouvy
 - ☐ 3 roky po uzavření této smlouvy
 - ☐ 5 let po uzavření této smlouvy
 - ☐ 10 let po uzavření této smlouvy
(z důvodu utajení v něm obsažených informací)
4. Nevýdělečné zveřejňování díla nabyvatelem v souladu s ustanovením § 47b zákona č. 111/ 1998 Sb., v platném znění, nevyžaduje licenci a nabyvatel je k němu povinen a oprávněn ze zákona.

Článek 3

Závěrečná ustanovení

1. Smlouva je sepsána ve třech vyhotoveních s platností originálu, přičemž po jednom vyhotovení obdrží autor a nabyvatel, další vyhotovení je vloženo do VŠKP.
2. Vztahy mezi smluvními stranami vzniklé a neupravené touto smlouvou se řídí autorským zákonem, občanským zákoníkem, vysokoškolským zákonem, zákonem o archivnictví, v platném znění a popř. dalšími právními předpisy.
3. Licenční smlouva byla uzavřena na základě svobodné a pravé vůle smluvních stran, s plným porozuměním jejímu textu i důsledkům, nikoliv v tísní a za nápadně nevýhodných podmínek.
4. Licenční smlouva nabývá platnosti a účinnosti dnem jejího podpisu oběma smluvními stranami.

V Brně dne: 30. května 2008

.....
Nabyvatel

.....
Autor

Prohlášení

Prohlašuji, že svou diplomovou práci na téma Implementation and Test of a 2D-integral-equation MoM-algorithm for the Analysis of Power-Bus Structures on Printed Circuit Boards jsem vypracoval samostatně pod vedením vedoucího diplomové práce a s použitím odborné literatury a dalších informačních zdrojů, které jsou všechny citovány v práci a uvedeny v seznamu literatury na konci práce.

Jako autor uvedené diplomové práce dále prohlašuji, že v souvislosti s vytvořením této diplomové práce jsem neporušil autorská práva třetích osob, zejména jsem nezasáhl nedovoleným způsobem do cizích autorských práv osobnostních a jsem si plně vědom následků porušení ustanovení § 11 a následujících autorského zákona č. 121/2000 Sb., včetně možných trestněprávních důsledků vyplývajících z ustanovení § 152 trestního zákona č. 140/1961 Sb.

V Brně dne 30. května 2008

.....
podpis autora

Acknowledgement

I would like to thank Prof. Marco Leone for the professional education support during my staying at Institute for Fundamental Electrical Engineering and Electromagnetic Compatibility in Magdeburg. I am also indebted to Ing. Oliver Kröning who helped me to realize the experimental validation of results.

I would also like to thank Prof. Zbyněk Raida, who afforded me an opportunity to work on the numerical modeling in electromagnetism.

V Brně dne 30. května 2008

.....
podpis autora

Abstract

This work is focused on the analysis of power-bus structures on printed circuit boards using the solution algorithm based on 2D-integral-equation formulation in the frequency domain. The algorithm is implemented in Matlab and is capable to analyze the parallel-plate structure with arbitrary material parameters, polygonal shape and number of ports. As output the program provides the frequency dependent voltage distribution between the plates, voltage/current relations between the ports and the radiation diagram of the structure. In order to simulate populated power-bus structures, the resulting Z-matrix can be converted into the so-called Touchstone Format file, which allows us to embed the power-bus structure into a network analysis (e.g. in ANSOFT Designer). All results are validated using the existing analytical solution for the rectangular structure, using a full-wave solver and by practical experiment.

Key words: 2D integral equation; Green's functions; power-bus structure; contour integral method (CIM); frequency domain analysis.

Abstrakt

Tato práce se zabývá analýzou power-bus struktur využitím metody založené na formulaci problému 2D hraniční integrální rovnicí ve frekvenční oblasti. Uvedená metoda byla implementována v Matlabu. Program umožňuje analyzovat obecné polygonální power-bus struktury s možností nastavení parametrů substrátu a libovolného počtu a umístění budících portů. Výstupem programu je frekvenční závislost rozložení elektrického pole mezi deskami struktury, vztahy mezi porty struktury vyjádřené např. impedanční maticí a vyzařovací diagram. Dále byla implementována možnost převodu výsledné impedanční matice do tzv. Touchstone formátu, pomocí něhož je možné modelovat analyzované struktury jako obecné N-porty (např. v ANSOFT Designeru), což umožňuje analýzu power-bus struktur s dalšími obvodovými prvky. Výsledky byly ověřeny pomocí existujících analytických vztahů pro jednoduché obdélníkové struktury, využitím komerčního simulačního programu a praktickým experimentem.

Klíčová slova: 2D integrální rovnice; Greenovy funkce; power-bus struktury; metoda hraničních prvků (MHP); analýza ve frekvenční oblasti

Abbreviations and symbols

CIM - Contour Integral Method, BEM - Boundary Element Method, FD - Frequency Domain, MSE - Mean Square Error, PCB - Printed Circuit Board, IC - Integrated Circuit, PEC - Perfect Electric Conductor, FDTD - Finite Difference-Time Domain, CEMPIE - Circuit Extraction-Mixed Potential Integral Equation

E - electric field intensity	ε_0 - electric permittivity of free space
H - electric field intensity	ε_r - relative permittivity (dielectric const.)
B - magnetic flux density	μ_0 - magnetic permeability of free space
D - electric flux density	μ_r - relative permeability
A - vector potential	∇ - Hamiltonian operator
ϕ - scalar potential	∇^2 - Laplacian operator
\mathbf{i}_s - surface current density	\sim - denotes spectral domain
r_s - surface charge density	r, r₀ - position vectors (observer, source)
k - wave vector	d - height of the substrate
k - wave number	I - electric current
λ - wavelength	V - electric voltage
ω - angular frequency	$J_n(\cdot)$ - Bessel function of order n
f - frequency	$H_n(\cdot)$ - Hankel function of order n
j - imaginary unit	$G(\cdot)$ - Green's function
c_0, c - speed of light (vacuum, dielectric)	$\delta(\cdot)$ - delta function
σ - conductivity	C - boundary contour
t - skin depth	D - 2D region bounded by C
$\tan\delta$ - loss tangent of the material	n - normal vector
Z - impedance matrix	u_{ij}, h_{ij} - matrix elements
Y - admittance	U, H - matrices

Bibliographic quotation:

ŠTUMPF, M. *Implementation and Test of a 2D-integral equation MoM-Algorithm for the Analysis of Power-Bus Structures on Printed Circuit Boards*. Brno: Vysoké učení technické v Brně, Fakulta elektrotechniky a komunikačních technologií, 2008. 49 s. Vedoucí diplomové práce prof. Dr.-Ing. Marco Leone.

Contents

1	Introduction	5
2	Electromagnetic Fundamentals.....	5
2.1	The Helmholtz Equation	5
2.2	Green's Theorems	8
2.3	The Unit Source in the Two Dimensions	8
2.4	Formulation of a Contour Integral Equation	10
2.5	Green's Function	12
3	Numerical Approach.....	15
3.1	Line Integrals.....	16
3.2	Derivation of Transfer Parameters	18
3.2.1	<i>One-Port Circuit</i>	18
3.2.2	<i>Two-Port Circuit</i>	21
3.2.3	<i>Multi-Port Circuit</i>	23
3.3	Computation of the Radiation Diagram.....	26
3.4	Implementation and the Program Structure	27
3.5	Circuit Level Simulation	28
4	Results	28
4.1	One-Port Rectangular Power-Bus Structure.....	28
4.2	One-Port Arbitrarily Shaped Power-Bus Structure	32
4.3	Accuracy and Computational Demands of the Implemented Algorithm.....	36
4.4	Matlab Program vs. ANSOFT Designer.....	38
5	Experimental Validation.....	42
6	Conclusion.....	46
7	References	47
8	Appendix	48

1 Introduction

A power-bus structure serves as the charge storage for the integrated circuits (IC) on a printed circuit board (PCB), reducing the switching noise, which rises from the changing between low and high states of the digital outputs of ICs. The minimizing of the switching noise ensures the signal integrity on the PCB and the reduction of the radiated electromagnetic interferences (EMI). In order to reduce the electromagnetic radiation of the power-bus structure, we are trying to avoid structural resonances, where the input impedance increases. For these reasons it is important to compute the voltage/current relations between the ports of the power-bus structure [1].

Recently, many papers have focused on the modeling of power-bus structures. One part of these methods, limited to the rectangular structure, is based on an analytical resonator model of the parallel plate structure [1]. Other classes of numerical approaches are based on full-wave methods as finite difference time domain method (FDTD) [9], or on the circuit extraction based on mixed-potential integral equation (CEMPIE) [10].

In the following chapters, the power-bus structure is analyzed using a numerical method based on a solving 2D boundary integral equation [4]. The main advantage of this approach is the high computational efficiency. All mathematical details of the numerical method will be carried out and the results will be compared with the existing analytical solutions for the simple shapes of power plate, with the results obtained from commercial software and with measurements.

2 Electromagnetic Fundamentals

Before we start with the analysis of the power bus-structures, the problem has to be mathematically described. The problem of the analysis of the parallel plate structures will be formulated as a boundary-value problem. The boundary-value problem is then reformulated to a 2D boundary integral equation and subsequently solved by the contour integral method (CIM) also known as the boundary element method (BEM) [4].

2.1 The Helmholtz Equation

The main subject of this thesis is the high-frequency analysis of a double-plate structure, as depicted in Fig. 1. The double-plate structure consists of a thin conductor of an arbitrary shape placed above the ground plane. The periphery of the structure is open. The circuit is excited at vertical ports by the current source I_0 , which represents the noise current injected in the power-bus structure by the supply pin of IC [1]. The material between power and ground plane is assumed to be isotropic and homogeneous. Only the small dielectric and conductor losses are considered. These losses are included in the complex wave number k as follows [1]:

$$k \approx k' - jk'', \quad \text{for } k' \ll k''$$

where

$$k' = k_0 \sqrt{\epsilon_r},$$
$$k'' = \frac{k'}{2} \left(\tan \delta + \frac{t}{d} \right).$$

where $k_0 = \omega/c_0$ is the wave number in the free space, c_0 is the speed of light in the vacuum and ω denotes the angular frequency. Next, the relative permittivity of the substrate is denoted as ϵ_r , and d denotes the distance between plates. The skin depth t is given as [1]:

$$t = \sqrt{\frac{2}{\omega\mu_0\sigma}},$$

where σ is the conductivity of the plates and μ_0 the magnetic permeability.

The distance between power plate and ground plane d is usually much smaller than the considered wavelengths, it means that condition $d \ll \lambda$ holds. Hence we can, under

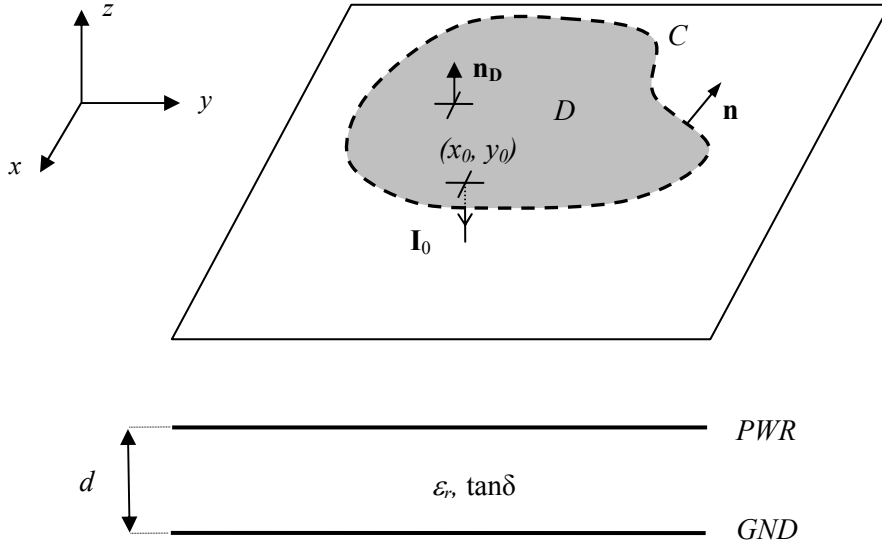


Fig. 1: Double-plate power bus structure

this condition, consider that all changes of the fields in the z -direction are zero: $\partial/\partial z = 0$. Since the power plate is assumed to be perfect electric conductor (PEC), the following conditions must be satisfied [3]:

$$\mathbf{n}_D \times \mathbf{H} = \mathbf{i}_s, \quad (1a)$$

$$\mathbf{n}_D \times \mathbf{E} = \mathbf{0}, \quad (1b)$$

$$\mathbf{n}_D \cdot \mathbf{D} = \rho_s, \quad (1c)$$

$$\mathbf{n}_D \cdot \mathbf{B} = 0, \quad (1d)$$

where $\mathbf{n}_D = (0, 0, 1)$ denotes the unit normal vector to the region D , \mathbf{E} and \mathbf{H} are the electric and magnetic field intensities, \mathbf{D} and \mathbf{B} denote the electric and magnetic flux densities, respectively. Next, \mathbf{i}_s and ρ_s denote the surface current and charge densities, respectively. Under these boundary conditions we obtain $H_z = E_x = E_y = 0$. When the time-harmonic regime $e^{j\omega t}$ is adopted, Faraday's and Ampere's law in the appropriate form can be written as follows [3]:

$$\bar{\nabla} \times \mathbf{E} = -j\omega\mu\mathbf{H}, \quad (2a)$$

$$\bar{\nabla} \times \mathbf{H} = j\omega\epsilon\mathbf{E}. \quad (2b)$$

After substituting above mentioned presumptions, equations (2) are simplified as [4]:

$$\frac{\partial E_z}{\partial y} = -j\omega\mu H_x, \quad (3a)$$

$$\frac{\partial E_z}{\partial x} = j\omega\mu H_y, \quad (3b)$$

$$\frac{\partial H_y}{\partial x} - \frac{\partial H_x}{\partial y} = j\omega\epsilon E_z. \quad (3c)$$

From the equations (3), after straightforward modifications, the following two-dimensional Helmholtz equation can be obtained [4]:

$$(\nabla_T^2 + k^2)E_z = 0, \quad (4a)$$

where $\nabla_T^2 = \partial^2 / \partial x^2 + \partial^2 / \partial y^2$ and k denotes the wave number. The problem to be solved is not fully defined until the boundary conditions along the periphery contour C are determined. To find the appropriate boundary condition, let suppose first that no external ports are connected to the periphery of the structure. In this case, there is no current flowing across the periphery. Hence according to equation (1a) the magnetic field lines are perpendicular to the contour C . From equations (3a) and (3b) is further clear, that the gradient of the electric field is normal to the magnetic field \mathbf{H} . Consequently, the gradient of the electric field is perpendicular to the outward normal \mathbf{n} on the contour C :

$$\frac{\partial E_z}{\partial n} = \bar{\nabla}_T E_z \cdot \mathbf{n} = 0 \quad \text{on } C. \quad (4b)$$

If the ports are connected to the periphery, then current flows into the circuit and the previous condition is not fulfilled. The corresponding boundary condition can be obtained with the help of equations (1a) and (3) as follows:

$$\frac{\partial E_z}{\partial n} = \bar{\nabla}_T E_z \cdot \mathbf{n} = -j\omega\mu \mathbf{i}_s \cdot \mathbf{n} = -j\omega\mu i_{sn} \quad \text{on } C, \quad (4c)$$

After integration of the electric field intensity E_z between the power and ground planes we obtain the high-frequency voltage $V = E_z d$. Using this voltage, the equations (4) can be rewritten [4]:

$$(\nabla_T^2 + k^2)V = 0 \quad \text{in } D, \quad (5a)$$

$$\frac{\partial V}{\partial n} = 0 \quad \text{on } C \quad (\text{ports absent}), \quad (5b)$$

$$\frac{\partial V}{\partial n} = -j\omega\mu d i_{sn} \quad \text{on } C \quad (\text{ports present}). \quad (5c)$$

The equations (5) represent the boundary-value problem, which can be solved by various methods. Most widely used methods are the finite-element method and finite-differences methods. The finite-element method is based upon the variational principles and the finite-difference method consists in replacement of partial derivatives with the appropriate finite differences. Both these methods are very versatile but computationally intensive. From this reason it is more convenient to use the contour integral method, because the dimension of the problem is reduced and the computational algorithms are more effective. This method is based upon the approximate solving of the integral equation related to the original boundary-value problem. To find the corresponding integral equation, Green's theorems have to be

applied and the appropriate resolving kernel (Green's function) has to be found. These problems are solved in the next chapters.

2.2 Green's Theorems

Let D be a simply connected region bounded by a "reasonable" closed contour C (e. g. piecewise smooth closed contour), and let \mathbf{U} be continuous differentiable vector field defined in D . For this vector field we can write the divergence theorem [2]:

$$\iint_D \bar{\nabla}_T \cdot \mathbf{U} dS = \oint_C \mathbf{U} \cdot \mathbf{n} ds, \quad (6)$$

where ds is an infinitesimal element of a contour C , $dS = dxdy$ denotes surface element and \mathbf{n} is the outward normal vector to the contour C . Next suppose that $\mathbf{U} = v \mathbf{V}$, where v is a scalar function of position and \mathbf{V} is a vector function. The divergence of \mathbf{U} then becomes:

$$\bar{\nabla}_T \cdot \mathbf{U} = \bar{\nabla}_T \cdot (v\mathbf{V}) = v\bar{\nabla}_T \cdot \mathbf{V} + \mathbf{V} \cdot \bar{\nabla}_T v.$$

If \mathbf{V} is an irrotational vector field, we can express it as the gradient of a scalar function u . The equation (6) can be then rewritten as:

$$\iint_D [v\bar{\nabla}_T \cdot (\bar{\nabla}_T u) + \bar{\nabla}_T u \cdot \bar{\nabla}_T v] dS = \oint_C v\bar{\nabla}_T u \cdot \mathbf{n} ds.$$

After noting that $\bar{\nabla}_T \cdot (\bar{\nabla}_T u) = \nabla_T^2 u$ and $\bar{\nabla}_T u \cdot \mathbf{n} = \partial u / \partial n$, we have Green's theorem in the first form:

$$\oint_C v \frac{\partial u}{\partial n} ds = \iint_D [v\nabla_T^2 u + \bar{\nabla}_T u \cdot \bar{\nabla}_T v] dS. \quad (7a)$$

The scalar functions v and w can be interchanged, and then we have:

$$\oint_C u \frac{\partial v}{\partial n} ds = \iint_D [u\nabla_T^2 v + \bar{\nabla}_T v \cdot \bar{\nabla}_T u] dS. \quad (7b)$$

After subtraction (7b) from (7a) the second form of Green's theorem is obtained [4]:

$$\oint_C \left(v \frac{\partial u}{\partial n} - u \frac{\partial v}{\partial n} \right) ds = \oint_C (v\bar{\nabla}_T u - u\bar{\nabla}_T v) \cdot \mathbf{n} ds = \iint_D [v\nabla_T^2 u - u\nabla_T^2 v] dS. \quad (8)$$

Note that $u, v \in C^2(D \cup C)$. This presumption can be more reduced, but here is no need.

2.3 The Unit Source in the Two Dimensions

The method described here, uses the idea of Green's functions: the field caused by a distributed source is simply obtained by the summing of the contributions of infinitesimal sources. In the following text, the notation $G(\mathbf{r}|\mathbf{r}_0)$ denotes the field at an observation point \mathbf{r} , caused by an infinitesimal source at a source point \mathbf{r}_0 . The crucial issue is to investigate the behavior of Green's function $G(\mathbf{r}|\mathbf{r}_0)$ in the close neighborhood of the source. Green's function in the immediate neighborhood of the source point will be denoted as $g(\rho)$, where ρ is a distance from a source point Q . The notation of the problem is depicted in Fig. 2, where the neighborhood of the source point Q is, for the sake of clarity, extended. It is well known, that Green's function is not continuous at $\mathbf{r} = \mathbf{r}_0$. This can be expressed, considering the solved problem (5) and unity source, as follows [4]:

$$(\nabla_T^2 + k^2)G(\mathbf{r} | \mathbf{r}_0) = \delta(\mathbf{r} - \mathbf{r}_0) \quad \text{in } D,$$

where $\delta(\cdot)$ denotes the delta function. Integrating this over the region B surrounding the source

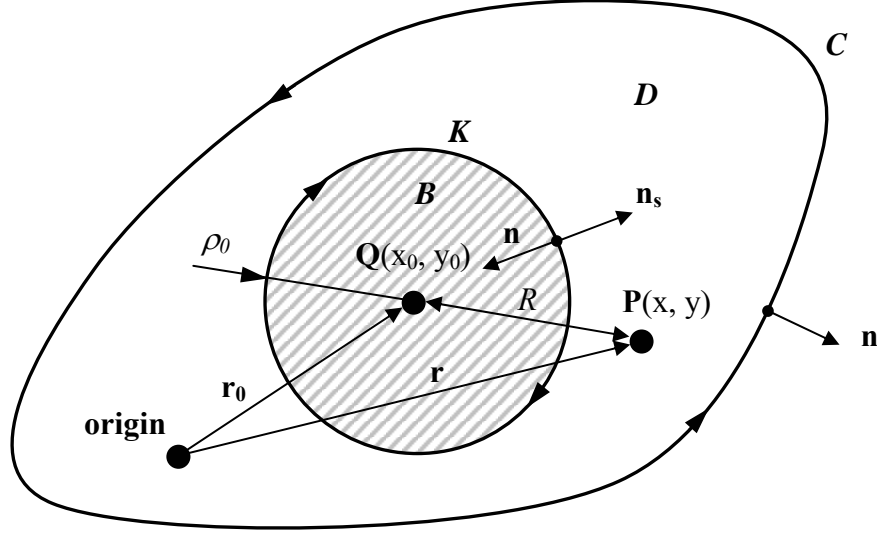


Fig. 2: Definition of a unit source

point Q , we obtain:

$$\iint_B \nabla_T^2 G \, dS + k^2 \iint_B G \, dS = 1.$$

The main contribution to the unity on the right side has the first integral on the left side, due to “stronger” singularity. Hence, under the limit $\rho_0 \rightarrow 0$, we can write:

$$\iint_B \nabla_T^2 g(\rho) \, dS = 1.$$

After using the Gauss theorem we arrive at the formulation of the yield q of a source:

$$q = \oint_K \nabla g(\rho) \cdot \mathbf{n}_s \, ds = 1, \quad (9)$$

where the orientation of the unit normal vector \mathbf{n}_s is depicted in Fig.2. It is obvious, that for unit source $q = 1$. Since g depends only on radial distance ρ from the source, the equation (9) can be modified as [2]:

$$q = \oint_K \frac{dg(\rho)}{d\rho} \, ds$$

The last integral can be easily computed as follows [2]:

$$q = \int_{-\pi}^{\pi} \frac{dg}{d\rho} \rho \, d\varphi = 2\pi\rho \frac{dg}{d\rho}.$$

Consequently, for a unit source in the two dimensions we obtain [2]:

$$\frac{dg}{d\rho} = -\frac{dg}{dn} = \frac{1}{2\pi} \frac{1}{\rho} \quad \text{and} \quad g = \frac{1}{2\pi} \ln \rho + \text{const}. \quad (10)$$

This result can be rewritten using the $G(\mathbf{r}|\mathbf{r}_0)$ as the limit:

$$\lim_{R \rightarrow 0} G(\mathbf{r} | \mathbf{r}_0) = \frac{1}{2\pi} \ln R, \quad (11)$$

where source/observer distance is given as: $R = |\mathbf{r} - \mathbf{r}_0|$. Green's function with the logarithmic singularity for a small argument will be discussed hereafter. Note that equation (11) is a fundamental solution of the Laplace equation. As will be shown later, the fundamental solution of the 2D Helmholtz equation, which satisfies the small-argument limit (11) are the zero order Hankel functions.

2.4 Formulation of a Contour Integral Equation

In the previous chapters we have formulated the boundary-value problem, definition of a unit source in the two dimensions and Green's theorems. With the help of the second form of Green's theorem (8) and the definition of a unit source (10), the boundary-value problem (5) can be reformulated to the corresponding contour integral.

If the source is outside the region D , then the both functions G and V and derivatives which appear are continuous throughout D , and the following equations hold:

$$(\nabla_T^2 + k^2)V = 0 \quad \text{and} \quad (\nabla_T^2 + k^2)G = 0 \quad \text{in } D.$$

When the second form of the Green theorem is applied, the following equality, in such case, can be written:

$$\iint_D (G \nabla_T^2 V - V \nabla_T^2 G) dS = \oint_C \left(G \frac{\partial V}{\partial n} - V \frac{\partial G}{\partial n} \right) ds = 0.$$

However, this is not actually our case because the source is considered to be inside the region D , as is depicted in Fig. 2. As was mentioned before, Green's function $G(\mathbf{r}|\mathbf{r}_0)$ is not continuous at the source point Q . To remedy this problem, we exclude an infinitesimally small circle, which surrounds the source point, from the domain of integration. Hence, according to Fig. 2, the domain of integration for a surface integral is $D - B$ and the line integral must be taken over both boundaries K and C with the orientation depicted in Fig. 3. The extraction of the small circle K from the domain of integration is depicted in Fig. 3. The integrals C_1 and C_2 , depicted in this figure, cancel each other. After this extraction we have:

$$\oint_K \left(G \frac{\partial V}{\partial n} - V \frac{\partial G}{\partial n} \right) ds + \oint_C \left(G \frac{\partial V}{\partial n} - V \frac{\partial G}{\partial n} \right) ds = 0. \quad (12)$$

For the first integral taken over small circle K , we make use of expressions for Green's functions in the immediate neighborhood of a source point (10), thus we get:

$$\frac{1}{2\pi} \oint_K \left(\ln \rho \frac{\partial V}{\partial n} + \frac{V}{\rho} \right) ds. \quad (13)$$

This integral can not be computed, because we do not know the values of a voltage V and its derivative $\partial V / \partial n$ on an infinitesimal circle K . Therefore we will make an estimate. For the first term in the previous integral following estimate holds:

$$\frac{1}{2\pi} \oint_K \ln \rho \frac{\partial V}{\partial n} ds \leq \frac{1}{2\pi} \max \left\{ \frac{\partial V}{\partial n} \right\} \oint_K \ln \rho ds = \max \left\{ \frac{\partial V}{\partial n} \right\} \rho \ln \rho.$$

Since the following limit holds:

$$\lim_{\rho \rightarrow 0} \rho \ln \rho = 0,$$

the contribution of the first term is zero and only the second term contributes to the integral over K [2]:

$$\frac{1}{2\pi} \oint_K \frac{V}{\rho} ds = \frac{V(Q)}{2\pi\rho_0} \oint_K ds = V(Q),$$

where $V(Q)$ denotes the voltage at the source point Q . Hence, the integral (12) can be then rewritten as:

$$V(Q) = \oint_C \left(V \frac{\partial G}{\partial n} - G \frac{\partial V}{\partial n} \right) ds. \quad (14)$$

From equation (14) can be computed rf voltage V at point Q in the region D , in terms of V and

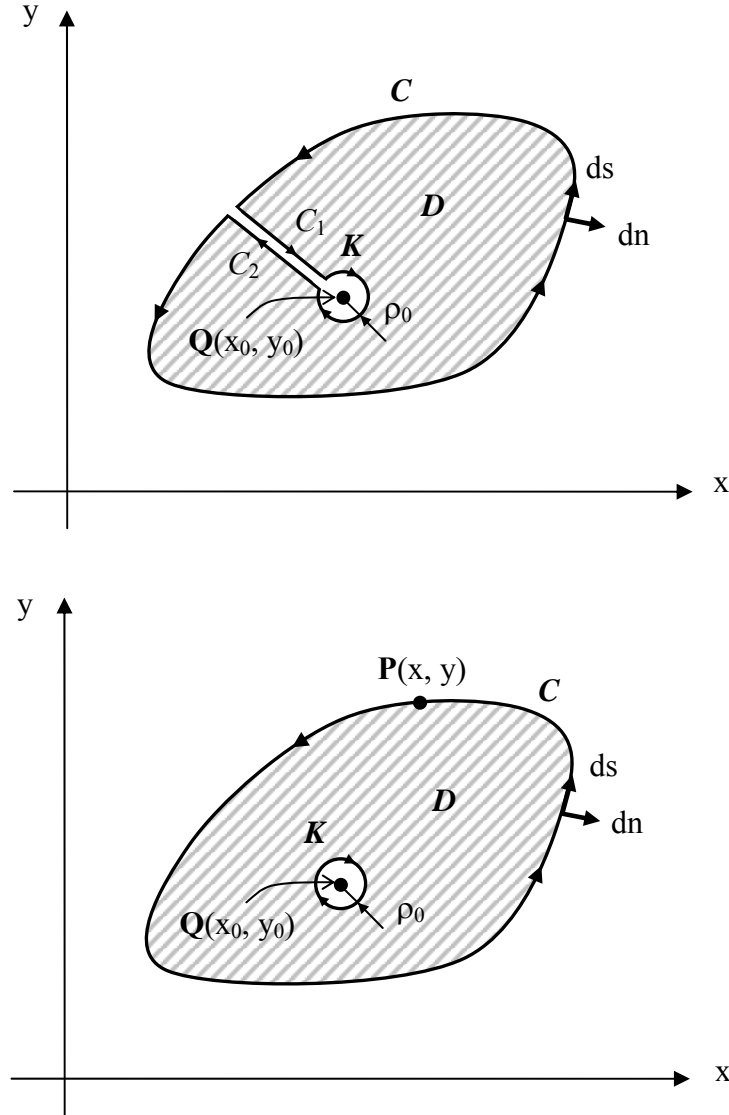


Fig. 3: Extraction of a singularity from region D

$\partial V/\partial n$ upon the contour C . However, the CIM requires the voltage V on contour C . In the next paragraphs, the transformation of equation (14), through the limit process $Q \in D \rightarrow Q' \in C$, is described.

The source point Q' is now set just on the contour depicted in Fig. 4. To find the rf potential at the point Q' we must exclude this point from the integration domain, because

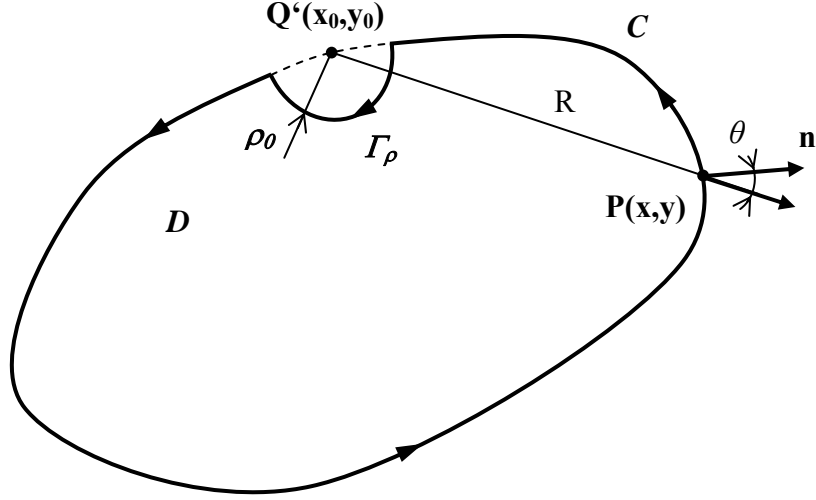


Fig. 4: Extraction of a singularity from contour C

Green's function $G(\mathbf{r}|\mathbf{r}_0)$ is not continuous here. The source point can be excluded by including a semicircular detour of infinitesimal radius. Similarly to the equation (12) we can write the following equation:

$$\int_{\Gamma_\rho} \left(G \frac{\partial V}{\partial n} - V \frac{\partial G}{\partial n} \right) ds + \int_{C-\Gamma_\rho} \left(G \frac{\partial V}{\partial n} - V \frac{\partial G}{\partial n} \right) ds = 0 .$$

As in the previous case, only the second term of the first integral over the semicircle contributes:

$$\frac{1}{2\pi} \int_{\Gamma_\rho} \frac{V}{\rho} ds = \frac{1}{2\pi} \pi V(Q') = \frac{V(Q')}{2} .$$

We therefore get the following expression:

$$V(Q') = 2 \int_{C-\Gamma_\rho} \left(V \frac{\partial G}{\partial n} - G \frac{\partial V}{\partial n} \right) ds .$$

By assuming limit $\rho_0 \rightarrow 0$, we can obtain equation for the potential at the point $Q' \in C$:

$$V(Q') = 2 \oint_C \left(V \frac{\partial G}{\partial n} - G \frac{\partial V}{\partial n} \right) ds , \quad (15)$$

where for the Green's function for $R \rightarrow 0$ holds the equation (11).

2.5 Green's Function

As was mentioned before, Green's function must satisfy the solved equation and in the source point Q must be singular as given in equation (11). Since the immediate neighborhood of the source depends only on the distance ρ from the source point, the Helmholtz equation for a desired Green's function is given as [5]:

$$\frac{1}{\rho} \frac{d}{d\rho} \left(\rho \frac{dG}{d\rho} \right) + k^2 G = 0. \quad (16)$$

The corresponding solution of equation (16) is the general cylindrical function of zero order $Z_0(kR)$. Because of the choice of the time harmonic regime $e^{j\omega t}$, the appropriate Green's function is the second Hankel function $H_0^{(2)}(kR)$. This solution of equation (16) then represents an outgoing cylindrical wave. The further step is to investigate the singularity of the second Hankel function at the origin. The value of the second Hankel function for a small argument is also useful in a numerical analysis of a problem discussed in the next chapters.

Following Sommerfeld [2], the second Hankel function of zero order can be written in the integral form written as:

$$H_0^{(2)}(kR) = \frac{1}{\pi} \int_{W_2} e^{jkR \cos w} dw, \quad (17a)$$

where the integration path is depicted in Fig. 5. For the sake of completeness, there are also depicted the integration paths for the Bessel function $J_n(\cdot)$ (W_0) and for the first Hankel

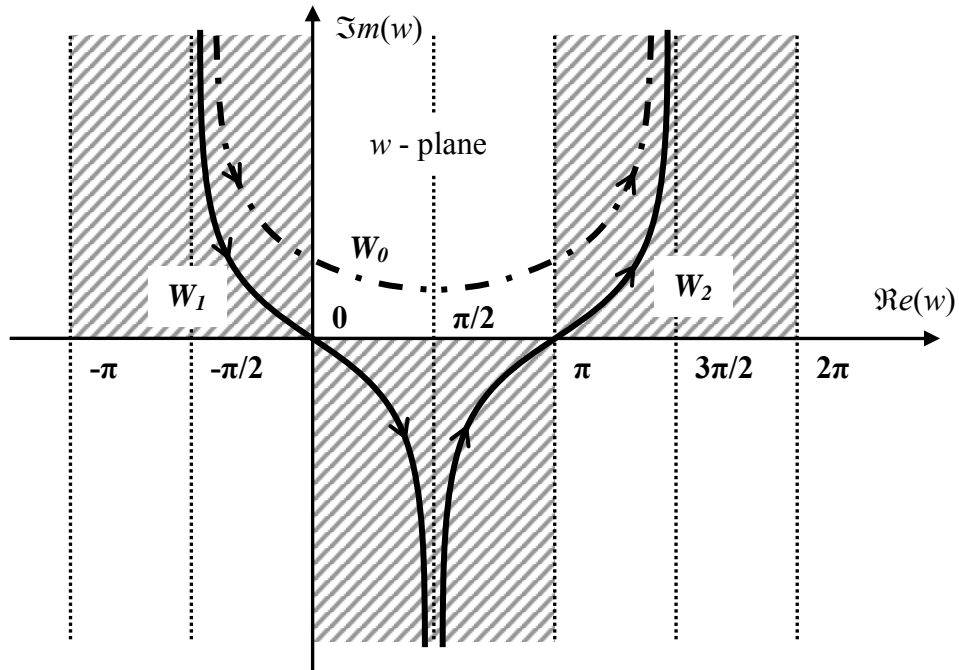


Fig. 5: Integration paths for the Bessel and Hankel functions

function $H_n^{(1)}(\cdot)$ (W_1). The shaded areas represent the convergent regions of the integral (17a). After following transformation of the previous integral [2]:

$$x = jkR \cos w,$$

the integration path W_2 is transformed into the path depicted in Fig. 6 and the integral (17a) then becomes:

$$H_0^{(2)}(kR) = -\frac{2j}{\pi} \int_{-\infty}^{-jp} \frac{e^x dx}{\sqrt{x^2 + k^2 R^2}}, \quad (17b)$$

where we use the change of the sign after integrating around the branch-point $-jkR$. After a few steps we obtain the following expression:

$$\lim_{R \rightarrow 0} H_0^{(2)}(kR) = -\frac{2j}{\pi} \ln(-jkR) + \frac{2j}{\pi} \int_{-\infty}^0 e^x \ln(2x) dx.$$

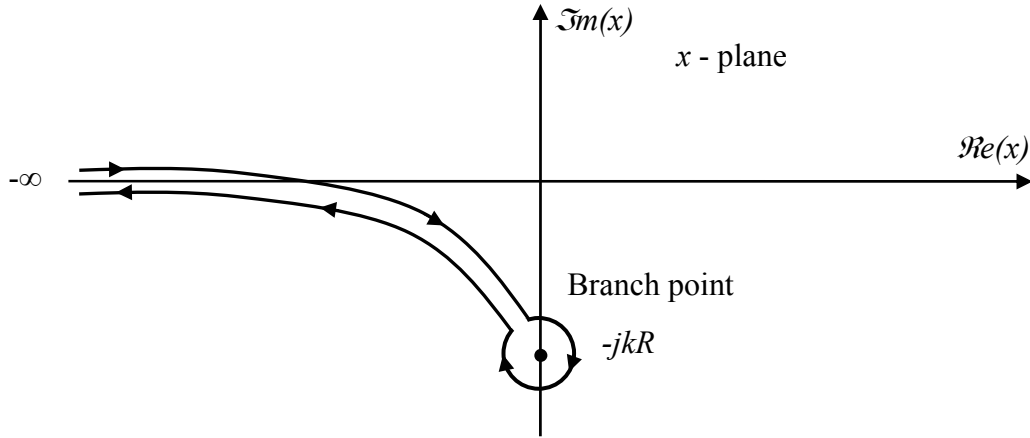


Fig. 6: Transformed integration path W_2

The previous expression can be rewritten in the following form:

$$\lim_{kR \rightarrow 0} H_0^{(2)}(kR) = 1 - \frac{2j}{\pi} \ln \frac{\gamma kR}{2}, \quad (18)$$

where $C = \ln \gamma = 0.5772\dots$ is Euler's constant. To make conformity between equations (11) and (18), Okoshi used the following expression [4]:

$$H_0^{(2)}(kR) \approx -\frac{2j}{\pi} \ln \frac{kR}{2} \quad \text{for } kR \ll 1. \quad (19)$$

Green's function for a unity source $G(\mathbf{r}|\mathbf{r}_0)$ can be then written, with the help of the second Hankel function, as follows:

$$G(\mathbf{r}|\mathbf{r}_0) = \frac{j}{4} H_0^{(2)}(kR). \quad (20)$$

When equation (20) is substituted into (14), the voltage at the source point Q in the region D is given as:

$$V(Q) = \frac{1}{4j} \oint_C \left(H_0^{(2)}(kR) \frac{\partial V}{\partial n} - V \frac{\partial H_0^{(2)}(kR)}{\partial n} \right) ds. \quad (21)$$

For the voltage at the source point at the point Q' , which lies on contour C , we get from equations (15) and (16):

$$V(Q') = \frac{1}{2j} \oint_C \left(H_0^{(2)}(kR) \frac{\partial V}{\partial n} - V \frac{\partial H_0^{(2)}(kR)}{\partial n} \right) ds. \quad (22)$$

The derivative of a voltage on periphery C is given by equation (5c) and for a derivative of the second Hankel function holds the following expression:

$$\frac{\partial H_0^{(2)}(kR)}{\partial n} = -k H_1^{(2)}(kR) \cos \theta,$$

where the angle θ is depicted in Fig. 4. Equation (22) then gives the voltage at the point upon the periphery using the rf-voltage $V(s)$ and rf-current $i_{sn}(s)$ along this periphery [4]:

$$V(Q') = \frac{1}{2j} \oint_C \left[k H_1^{(2)}(kR) V(s) \cos \theta - j \omega \mu d H_0^{(2)}(kR) i_{sn}(s) \right] ds, \quad (23)$$

where ds is the infinitesimal element of the contour C , R is the source/observer distance and i_{sn} denotes the surface current density flowing outwards along the periphery C . It is important to note, that contour C in the equation (23) can be multiply connected [4]. The equation (23) is usually called as Weber's solution for cylindrical waves and will be solved numerically in the following chapters.

3 Numerical Approach

The major task of this chapter is a numerical solution of the integral equation (23) derived in the previous chapter. The numerical method adopted here is applicable to an arbitrary circuit pattern. The first step in numerical solution of equation (23) is a division of the circuit periphery into N small segments depicted in Fig. 7. The center of each segment is represented as dot and called sampling point. The W_i denotes the width of i -th segment ($i = 1, 2, \dots, N$ and $N = m + n + M$) and m, n denote the number of elements of the inner circles. If we assume that rf voltage and current are constant over each segment, we can rewrite the equation (23), for the i -th segment ($1 \leq i \leq N$), as follows:

$$V_i = \frac{1}{2j} \sum_{j=1}^N \left(k V_j \int_{W_j} H_1^{(2)}(kR) \cos \theta ds - j \omega \mu d i_j \int_{W_j} H_0^{(2)}(kR) ds \right),$$

where V_j and i_j denote the rf voltage at the j -th sampling point and surface current density flowing outwards from the j -th port, respectively. Now we separate the voltage and current and we obtain:

$$V_i \left(1 - \frac{k}{2j} \int_{W_i} H_1^{(2)}(kR) \cos \theta ds \right) - \frac{k}{2j} \sum_{j=1, j \neq i}^N \left(V_j \int_{W_j} H_1^{(2)}(kR) \cos \theta ds \right) = -\frac{\omega \mu d}{2} \sum_{j=1}^N \left(i_j \int_{W_j} H_0^{(2)}(kR) ds \right).$$

Next we introduce the total current flowing into j -port as $I_j = -i_j W_j$. Then we can rewrite the solved integral equation to the system of linear equations in compact form [4]:

$$\sum_{j=1}^N u_{ij} V_j = \sum_{j=1}^N h_{ij} I_j \quad (i = 1, 2, \dots, N), \quad (24)$$

where

$$u_{ij} = \delta_{ij} - \frac{k}{2j} \int_{W_j} H_1^{(2)}(kR) \cos \theta ds, \quad (25a)$$

$$h_{ij} = \begin{cases} \frac{\omega \mu d}{2} \frac{1}{W_j} \int_{W_j} H_0^{(2)}(kR) ds & (i \neq j) \\ \frac{\omega \mu d}{2} \left[1 - \frac{2j}{\pi} \left(\ln \frac{\gamma k W_i}{4} - 1 \right) \right] & (i = j) \end{cases}. \quad (25b)$$

where δ_{ij} denotes Kronecker delta. The expressions for self-coupling terms ($i = j$) were obtained from the asymptotic expression (18). When the equation (24) is solved, the voltage

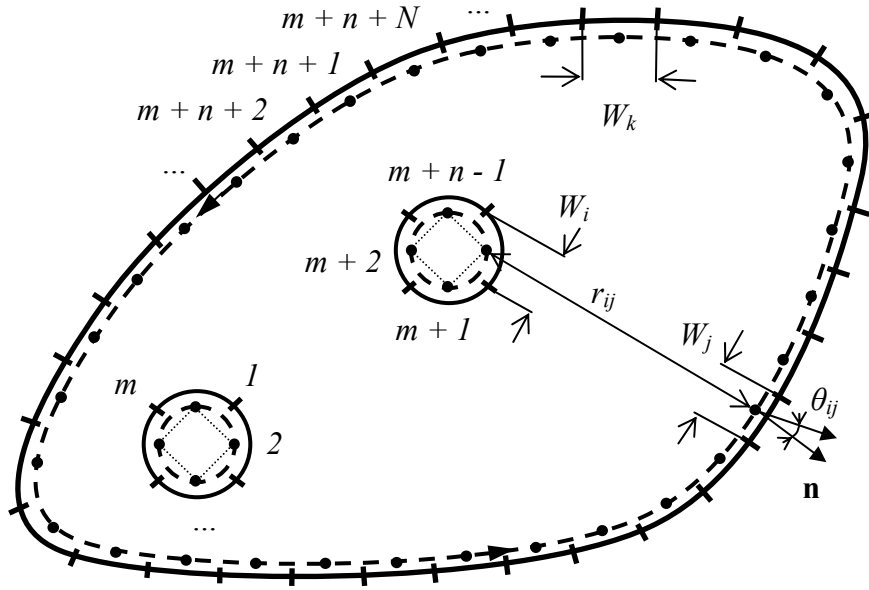


Fig. 7: Elements on the contour C

along the periphery of a circuit at each sampling point is obtained. The crucial issue is solving of the line integrals in (25) containing the Hankel functions along the segments. In the next chapters, we introduce the methods of solving these integrals. This problem should be solved with regard to accuracy and efficiency of resulting algorithm.

3.1 Line Integrals

The matrix elements u_{ij} and h_{ij} can be easily obtained from equations (25) without computing integrals as [4]:

$$u_{ij} = \delta_{ij} - \frac{k}{2j} H_1^{(2)}(kr_{ij}) W_j \cos \theta_{ij}, \quad (26a)$$

$$h_{ij} = \frac{\omega \mu d}{2} H_0^{(2)}(kr_{ij}), \quad (26b)$$

where θ_{ij} is an angle between the line connecting the centers of the i -th and j -th segments and the normal to the j -th segment. The matrix elements u_{ij} and h_{ij} are, in this simplest case, computed at the centre of i -th target element as the contribution of the j -th source element, under assumption of constant integrands in equations (25). However, the integrals can be computed more precisely by computing u_{ij} (or h_{ij}) at the centre of the i -th element by integrating the contributions of j -th element along W_j . Note that the most accurate procedure is the integrating the contributions from j -th elements along the target i -th element (not only at the centre of i -th element). In this thesis, we will take into account with regard the accuracy and the computational demands, the approximate expressions (26) and the more accurate ones, obtained by the integration along the j -th source element. Firstly, we will focus on expressions (26).

In Fig. 8 are depicted arbitrarily placed i -th and j -th segments limited by the points $[X_i, Y_i]$, $[X_{i+1}, Y_{i+1}]$ and $[X_j, Y_j]$, $[X_{j+1}, Y_{j+1}]$, respectively. The distance between the corresponding

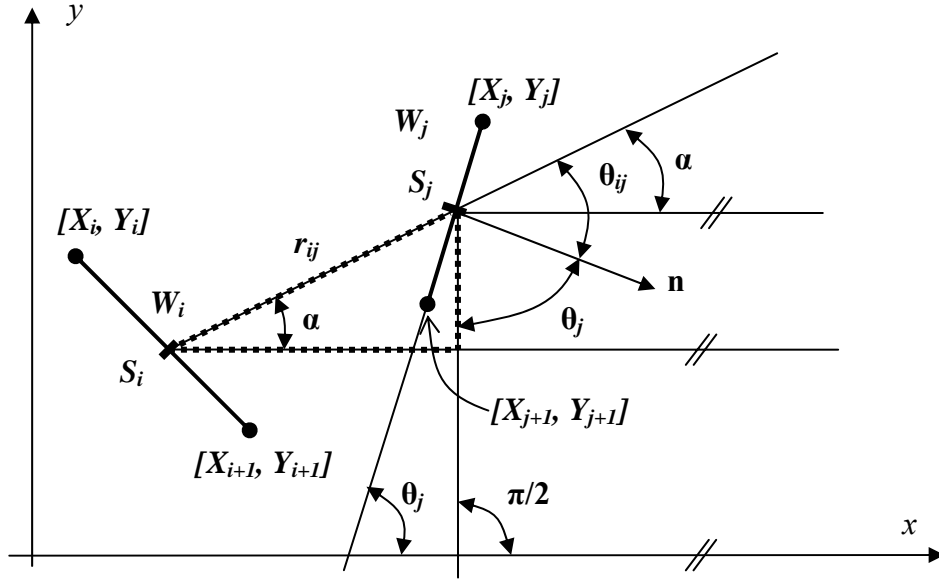


Fig. 8: Symbols used in the integration along the segments

sampling points at the centers of segments $S_i = [SX_i, SY_i]$ and $S_j = [SX_j, SY_j]$ is denoted as r_{ij} . Obviously, the width of i -th segment is given as:

$$W_i = \sqrt{(X_i - X_{i+1})^2 + (Y_i - Y_{i+1})^2} \quad (i = 1, 2, \dots, N).$$

Similarly, the distance between the depicted sampling points is given as:

$$r_{ij} = \sqrt{(SX_i - SX_j)^2 + (SY_i - SY_j)^2} \quad (i = 1, 2, \dots, N). \quad (27)$$

Since we can write the relation between angles depicted in Fig. 8 as:

$$\theta_{ij} - \alpha + \theta_j = \frac{\pi}{2},$$

the following expression holds:

$$\cos \theta_{ij} = \cos \alpha \sin \theta_j - \sin \alpha \cos \theta_j, \quad (28)$$

with

$$\begin{aligned} \cos \theta_j &= \frac{X_{j+1} - X_j}{W_j} \quad \text{and} \quad \sin \theta_j = \frac{Y_{j+1} - Y_j}{W_j}, \\ \cos \alpha &= \frac{SX_j - SX_i}{r_{ij}} \quad \text{and} \quad \sin \alpha = \frac{SY_j - SY_i}{r_{ij}}. \end{aligned}$$

These expressions can be substituted to the equations (26), and the matrix equation (24) can be solved.

For the more accurate computation of the matrix elements, we have to execute the integration along the j -th source elements. It is convenient to describe the j -th segment parametrically as $\mathbf{r}_j(t) = x_j(t)\mathbf{e}_x + y_j(t)\mathbf{e}_y$, with:

$$\left. \begin{aligned} x_j(t) &= X_j + t(X_{j+1} - X_j) \\ y_j(t) &= Y_j + t(Y_{j+1} - Y_j) \end{aligned} \right\} \quad t \in <0,1>,$$

where \mathbf{e}_x and \mathbf{e}_y are the basis vectors for two-dimensional Cartesian coordinates. The infinitesimal element of the parametrically described segment $\mathbf{r}_j(t)$ can be written as:

$$ds = \sqrt{\frac{d\mathbf{r}_j(t)}{dt} \frac{d\mathbf{r}_j(t)}{dt}} dt = W_j dt.$$

As a consequence of implementation of the parameter $t \in <0,1>$, the distance between the target and the source points (27) can be rewritten as:

$$r_{ij}(t) = \sqrt{(SX_i - x_j(t))^2 + (SY_i - y_j(t))^2} \quad (i = 1, 2, \dots, N). \quad (29)$$

Similarly, the equation (28) in the parametric form is given as:

$$\cos \theta_{ij}(t) = \cos \alpha(t) \sin \theta_j - \sin \alpha(t) \cos \theta_j, \quad (30)$$

with

$$\cos \alpha(t) = \frac{x_j(t) - SX_i}{r_{ij}(t)} \quad \text{and} \quad \sin \alpha(t) = \frac{y_j(t) - SY_i}{r_{ij}(t)}. \quad (31)$$

For the matrix elements u_{ij} and h_{ij} the following expressions can be obtained:

$$u_{ij} = \delta_{ij} - \frac{k}{2j} \int_{t=0}^1 H_1^{(2)}(kr_{ij}(t)) \cos \theta_{ij}(t) W_j dt \quad (i \neq j), \quad (32a)$$

$$h_{ij} = \frac{\omega \mu d}{2} \int_{t=0}^1 H_0^{(2)}(kr_{ij}(t)) dt \quad (i \neq j). \quad (32b)$$

The integrals (32) can be evaluated using some of the numerical methods, e.g. Gauss-Legendre method.

3.2 Derivation of Transfer Parameters

Once the matrix elements u_{ij} and h_{ij} are computed, the transfer voltage/current parameters can be derived. In the next subsections, the transfer parameters are derived for the one-port, two-port and multi-port power-bus structure. In the case of one-port and two-port structures, the transfer parameters are derived without the inversion of the matrix. Further, we will derive the matrix equations used for the evaluation of the voltages along and inside of the circuit periphery.

3.2.1 One-Port Circuit

In this section, the one port double-plate circuit with arbitrarily shaped power plate will be considered. As was mentioned before, the circuit is excited by the current source I_0 . Due this excitation at the position (x_0, y_0) , the voltage distribution $V(x, y)$ within the power-bus exists. We are interested in the input impedance $Z_{inp} = V(x_0, y_0)/I_0$. Another parameter which can be computed by the presented method is the voltage distribution along the periphery of the circuit. As is shown in [1], this distribution can be used to obtain the radiated fields of the power-bus structure.

We will start with the equation (24) in the appropriate form:

$$\mathbf{U} \cdot [V_0 \cdots V_0 \mid V_1 \ V_2 \cdots V_N]^T = \mathbf{H} \cdot \left[\frac{I_0}{m} \cdots \frac{I_0}{m} \mid 0 \ 0 \cdots 0 \right]^T, \quad (33)$$

where the elements of matrices \mathbf{U} and \mathbf{H} are given by the equations (26) or (32) and $(\cdot)^T$ denotes the transposition. Next, the injected current I_0 is uniformly divided into the m segments of the port, $V(x_0, y_0)$ is denoted as V_0 and the V_1, V_2, \dots, V_N denote the N voltages at the sampling points along the periphery of the circuit. The matrix equation (33) represents a system of $(m + N)$ scalar equations with $(N + 1)$ unknowns, therefore the matrices \mathbf{U} and \mathbf{H} should be reduced. The corresponding reduction is depicted in Fig. 9. The elements of the matrix bounded by the dotted rectangle are added together generating one element in the

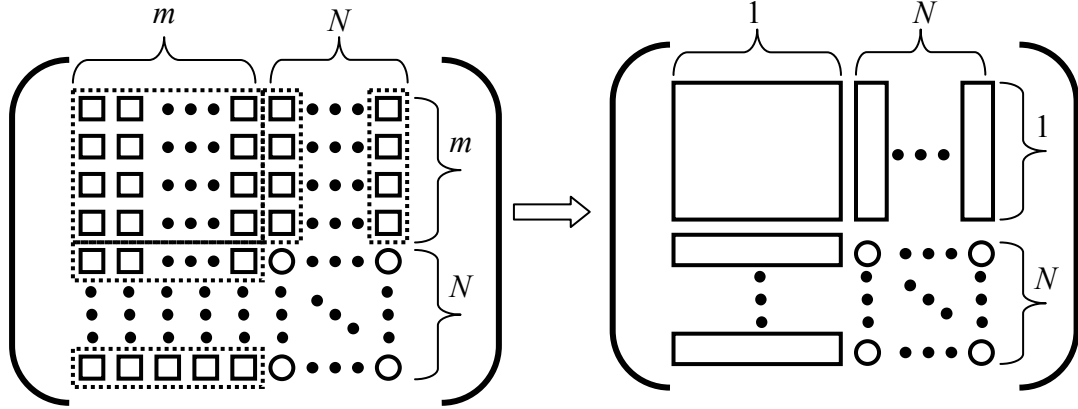


Fig. 9: Matrix reduction (one port circuit)

reduced matrix¹. After this reduction the following matrix equation can be obtained:

$$\mathbf{U}_R \cdot \begin{bmatrix} V_0 \\ V_1 \\ \vdots \\ V_N \end{bmatrix} = \mathbf{H}_R \cdot \begin{bmatrix} I_0 / m \\ 0 \\ \vdots \\ 0 \end{bmatrix}, \quad (34a)$$

where the subscript $(\cdot)_R$ denotes the reduced matrix. From the equation (34) we can obtain the desired parameters of the one port circuit. After substitution $I_0 = -Y_0 V_0$ to the equation (34), following system of the equations is obtained:

$$\left(\mathbf{U}_R + \frac{Y_0}{m} \mathbf{H}_R \right) \cdot \begin{bmatrix} V_0 \\ V_1 \\ \vdots \\ V_N \end{bmatrix} = \mathbf{0}. \quad (34b)$$

The system of algebraic equations (34b) has the nontrivial solution only if the determinant of the corresponding matrix is zero:

$$\det \left\{ \mathbf{U}_R + \frac{Y_0}{m} \mathbf{H}_R \right\} = 0. \quad (35)$$

¹ Suppose that the port is divided into the 3 segments, then the relation between the port and the 4th segment on C is given as: $V_0 \sum_{i=1}^3 \sum_{j=1}^3 u_{ij} + V_1(u_{14} + u_{24} + u_{34} + u_{44}) = (I_0 / m) \sum_{i=1}^3 \sum_{j=1}^3 h_{ij}$, which explains the reduction depicted in Fig. 9.

The equation (35) can be rewritten in the extended form as follows:

$$\begin{vmatrix} u_{1,1} + (Y_0 / m)h_{1,1} & u_{1,2} & \cdots & u_{1,N+1} \\ u_{2,1} + (Y_0 / m)h_{2,1} & u_{2,2} & \cdots & u_{2,N+1} \\ \vdots & \vdots & \ddots & \vdots \\ u_{N+1,1} + (Y_0 / m)h_{N+1,1} & u_{N+1,2} & \cdots & u_{N+1,N+1} \end{vmatrix} = 0.$$

This equation gives, after a few steps of algebra [11], the voltage/current relation at the position of the port (x_0, y_0) :

$$Y_0 = -m \frac{C'}{A'},$$

with

$$C' = \begin{vmatrix} u_{1,1} & u_{1,2} & \cdots & u_{1,N+1} \\ u_{2,1} & u_{2,2} & \cdots & u_{2,N+1} \\ \vdots & \vdots & \ddots & \vdots \\ u_{N+1,1} & u_{N+1,2} & \cdots & u_{N+1,N+1} \end{vmatrix},$$

and

$$\frac{Y_0}{m} A' = \begin{vmatrix} h_{1,1} & u_{1,2} & \cdots & u_{1,N+1} \\ h_{2,1} & u_{2,2} & \cdots & u_{2,N+1} \\ \vdots & \vdots & \ddots & \vdots \\ h_{N+1,1} & u_{N+1,2} & \cdots & u_{N+1,N+1} \end{vmatrix},$$

where the parameters are dependent on the geometry of the power bus-structure and on the operational frequency.

The input impedance of the power bus structure can be also simply derived from the equation (34a), by noting that impedance matrix of the circuit is given as:

$$\mathbf{Z} = \mathbf{U}_R^{-1} \cdot \mathbf{H}_R. \quad (36)$$

Thus, equation (34) can be rewritten as:

$$\begin{bmatrix} V_0 \\ V_1 \\ \vdots \\ V_N \end{bmatrix} = \begin{bmatrix} z_{1,1} & z_{1,2} & \cdots & z_{1,N+1} \\ z_{2,1} & z_{2,2} & \cdots & z_{2,N+1} \\ \vdots & \vdots & \ddots & \vdots \\ z_{N+1,1} & z_{N+1,2} & \cdots & z_{N+1,N+1} \end{bmatrix} \cdot \begin{bmatrix} I_0 / m \\ 0 \\ \vdots \\ 0 \end{bmatrix}, \quad (37)$$

where z_{ij} are the elements of the impedance matrix \mathbf{Z} . The input impedance can be easily obtained from this system of scalar equations as follows:

$$Z_{inp} = \frac{V_0}{I_0} = \frac{z_{1,1}}{m}. \quad (38a)$$

The second approach of calculation of the input impedance of the power-bus structure demands the computation of the inverse matrix \mathbf{U}_R^{-1} , which is usually more time consuming than the computation of two determinants in the first approach.

Once the input impedance of the power-bus structure is computed, the voltage at each sampling point along the periphery of the circuit can be evaluated. The voltage V_0 is suitably chosen, and the voltages V_1, V_2, \dots, V_N along the periphery are obtained by solving the system of scalar equations (37) or (34b) (without requirement of matrix inversion). From the system of equations (37) we obtain following system:

$$\begin{bmatrix} V_1 \\ V_2 \\ \vdots \\ V_N \end{bmatrix} = \frac{I_0}{m} \begin{bmatrix} z_{2,1} \\ z_{3,1} \\ \vdots \\ z_{N+1,1} \end{bmatrix}. \quad (38b)$$

The number of elements of the port m must be greater than 3 to make the contour closed. Obviously, as m increases the approximation of the circular port is more accurate, whereas the computational demands increase.

3.2.2 Two-Port Circuit

This section is focused on the analysis of the power-bus structures, which are excited by the two current sources I_{01} and I_{02} at the positions (x_{01}, y_{02}) and (x_{02}, y_{02}) , respectively. As in the previous section, we are interested in the current/voltages relations between the ports.

The matrix equation (24) for the two port circuit has the following:

$$\mathbf{U} \cdot [V_{01} \dots V_{01} \ V_{02} \dots V_{02} \mid V_1 \ V_2 \dots V_N]^T = \mathbf{H} \cdot \left[\frac{I_{01}}{m} \dots \frac{I_{01}}{m} \ \frac{I_{02}}{n} \dots \frac{I_{02}}{n} \mid 0 \ 0 \dots 0 \right]^T, \quad (39)$$

where the elements of the matrices \mathbf{U} and \mathbf{H} can be computed using the expressions (26) or (32) and superscript $(.)^T$ denotes the transposition. In general, the injected current of the first port I_{01} , is uniformly distributed among the m segments and the current I_{02} of the second port is uniformly distributed among the n segments. The voltages V_1, V_2, \dots, V_N denote the voltages

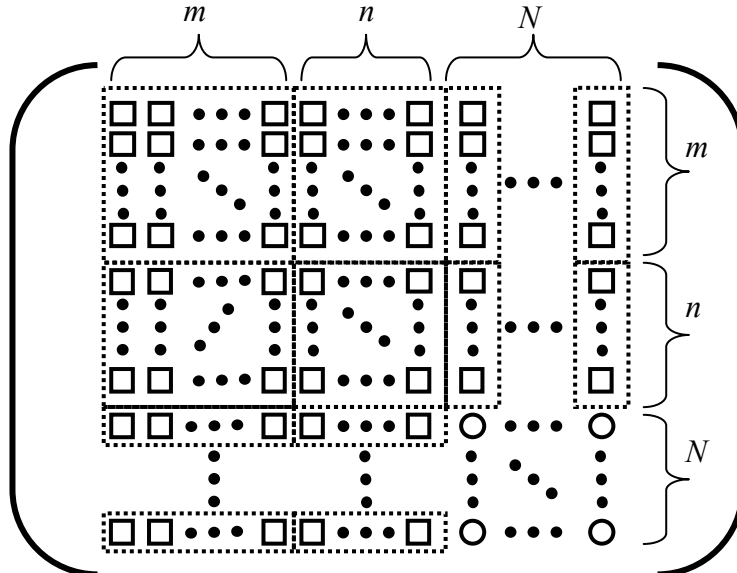


Fig. 10: Matrix reduction (two port circuit)

along the periphery of the circuit and V_{01} and V_{02} are the voltages at positions of the first and the second port, respectively. The system of $(m + n + N)$ equations (39) contains $(N + 2)$ variables and should be reduced. The matrix reduction for the two port circuit is depicted in Fig. 10. As in the previous section, the elements of the matrix \mathbf{U} or \mathbf{H} bounded by the

rectangles are added together and this sum generates a new element in the reduced matrix \mathbf{U}_R or \mathbf{H}_R . After execution denoted operations, we obtain the system of $(N+2)$ scalar equations:

$$\mathbf{U}_R \cdot \begin{bmatrix} V_{01} \\ V_{02} \\ V_1 \\ \vdots \\ V_N \end{bmatrix} = \mathbf{H}_R \cdot \begin{bmatrix} I_{01}/m \\ I_{02}/n \\ 0 \\ \vdots \\ 0 \end{bmatrix}. \quad (40a)$$

If we substitute $I_{01} = -Y_{01} V_{01}$ and $I_{02} = -Y_{02} V_{02}$ to the matrix equation (40a), the following expression can be obtained:

$$\left(\mathbf{U}_R + \frac{Y_{01}}{m} \mathbf{H}_R^{(1)} + \frac{Y_{02}}{n} \mathbf{H}_R^{(2)} \right) \cdot \begin{bmatrix} V_{01} \\ V_{02} \\ V_1 \\ \vdots \\ V_N \end{bmatrix} = \mathbf{0}, \quad (40b)$$

where the superscript denote nonzero column of the \mathbf{H}_R matrix:

$$\mathbf{H}_R^{(1)} = \begin{bmatrix} h_{1,1} & 0 & \cdots & 0 \\ h_{2,1} & 0 & \cdots & 0 \\ \vdots & \vdots & \ddots & \vdots \\ h_{N+2,1} & 0 & \cdots & 0 \end{bmatrix}, \quad \mathbf{H}_R^{(2)} = \begin{bmatrix} 0 & h_{1,2} & \cdots & 0 \\ 0 & h_{2,2} & \cdots & 0 \\ \vdots & \vdots & \ddots & \vdots \\ 0 & h_{N+2,2} & \cdots & 0 \end{bmatrix}.$$

The system of $(N+2)$ scalar equations has the nontrivial solution only if the determinant of the corresponding matrix is zero:

$$\det \left\{ \mathbf{U}_R + \frac{Y_{01}}{m} \mathbf{H}_R^{(1)} + \frac{Y_{02}}{n} \mathbf{H}_R^{(2)} \right\} = 0.$$

After simple algebraic operations we obtain the bilinear expression for the input impedance:

$$-Y_{01} = \frac{m \cdot n \cdot C' + m \cdot D' \cdot Y_{02}}{n \cdot A' + B' \cdot Y_{02}}, \quad (41)$$

with

$$A' = \begin{vmatrix} h_{1,1} & u_{1,2} & \cdots & u_{1,N+2} \\ h_{2,1} & u_{2,2} & \cdots & u_{2,N+2} \\ \vdots & \vdots & \ddots & \vdots \\ h_{N+2,1} & u_{N+2,2} & \cdots & u_{N+2,N+2} \end{vmatrix}, \quad B' = \begin{vmatrix} h_{1,1} & h_{1,2} & u_{1,3} & \cdots & u_{1,N+2} \\ h_{2,1} & h_{2,2} & u_{2,3} & \cdots & u_{2,N+2} \\ h_{3,1} & h_{3,2} & u_{3,3} & \cdots & u_{3,N+2} \\ \vdots & \vdots & \vdots & \ddots & \vdots \\ h_{N+2,1} & h_{N+2,2} & u_{N+2,3} & \cdots & u_{N+2,N+2} \end{vmatrix},$$

and

$$C' = \begin{vmatrix} u_{1,1} & u_{1,2} & \cdots & u_{1,N+2} \\ u_{2,1} & u_{2,2} & \cdots & u_{2,N+2} \\ \vdots & \vdots & \ddots & \vdots \\ u_{N+2,1} & u_{N+2,2} & \cdots & u_{N+2,N+2} \end{vmatrix}, \quad D' = \begin{vmatrix} u_{1,1} & h_{1,2} & u_{1,3} & \cdots & u_{1,N+2} \\ u_{2,1} & h_{2,2} & u_{2,3} & \cdots & u_{2,N+2} \\ u_{3,1} & h_{3,2} & u_{3,3} & \cdots & u_{3,N+2} \\ \vdots & \vdots & \vdots & \ddots & \vdots \\ u_{N+2,1} & h_{N+2,2} & u_{N+2,3} & \cdots & u_{N+2,N+2} \end{vmatrix}.$$

The ABCD parameters are easy to obtain by the following substitutions:

$$A'' = nA', B'' = B', C'' = mnC', D'' = mD',$$

and regarding the reciprocity condition [4]:

$$\begin{bmatrix} A & B \\ C & D \end{bmatrix} = \frac{1}{\sqrt{A''D'' - B''C''}} \begin{bmatrix} A'' & B'' \\ C'' & D'' \end{bmatrix}.$$

As in the previous section, another way of computing transfer parameters through the matrix inversion exists. The impedance matrix \mathbf{Z} is computed according to (36), and the equation (40a) can be rewritten as:

$$\begin{bmatrix} V_{01} \\ V_{02} \\ V_1 \\ \vdots \\ V_N \end{bmatrix} = \begin{bmatrix} z_{1,1} & z_{1,2} & z_{1,3} & \cdots & z_{1,N+2} \\ z_{2,1} & z_{2,2} & z_{2,3} & \cdots & z_{2,N+2} \\ z_{3,1} & z_{3,2} & z_{3,3} & \cdots & z_{3,N+2} \\ \vdots & \vdots & \vdots & \ddots & \vdots \\ z_{N+2,1} & z_{N+2,2} & z_{N+2,3} & \cdots & z_{N+2,N+2} \end{bmatrix} \cdot \begin{bmatrix} I_{01}/m \\ I_{02}/n \\ 0 \\ \vdots \\ 0 \end{bmatrix}. \quad (42)$$

Thus, the voltage/current relations between ports can be written as:

$$\begin{bmatrix} V_{01} \\ V_{02} \end{bmatrix} = \begin{bmatrix} z_{1,1}/m & z_{1,2}/n \\ z_{2,1}/m & z_{2,2}/n \end{bmatrix} \cdot \begin{bmatrix} I_{01} \\ I_{02} \end{bmatrix}. \quad (43a)$$

Analogous to the previous section, the voltages along the periphery of the circuit can be computed from the matrix equation (40b) or (42). From the matrix equation (42) we obtain following expressions for the voltages at the sampling points along the circuit periphery:

$$\begin{bmatrix} V_1 \\ V_2 \\ \vdots \\ V_N \end{bmatrix} = \begin{bmatrix} z_{3,1}/m & z_{3,2}/n \\ z_{4,1}/m & z_{4,2}/n \\ \vdots & \vdots \\ z_{N+2,1}/m & z_{N+2,2}/n \end{bmatrix} \cdot \begin{bmatrix} I_{01} \\ I_{02} \end{bmatrix}, \quad (43b)$$

We have derived the expressions for the ABCD parameters and the Z-parameters of the two-port power-bus structure. In the next section, we will derive the Z-matrix for the general multi-port power-bus structure.

3.2.3 Multi-Port Circuit

In this chapter, the multi-port power-bus structure with arbitrarily shaped power plate is considered. We suppose, that analyzed structure is excited by the P current sources I_{01}, \dots, I_{0P} . Each of these ports is divided into m segments. Along the periphery of the circuit is N sampling points. Thus, the matrix equation (24) has the following form:

$$\begin{aligned} \mathbf{U} \cdot [V_{01} \cdots V_{01} \ V_{02} \cdots V_{02} \cdots V_{oP} \cdots V_{oP} \mid V_1 \ V_2 \cdots V_N]^T = \\ = \mathbf{H} \cdot \left[\frac{I_{01}}{m} \cdots \frac{I_{01}}{m} \ \frac{I_{02}}{m} \cdots \frac{I_{02}}{m} \cdots \frac{I_{oP}}{m} \cdots \frac{I_{oP}}{m} \mid 0 \ 0 \cdots 0 \right]^T, \end{aligned} \quad (44)$$

where superscript $(.)^T$ denotes the transposition and the elements of matrices \mathbf{U} and \mathbf{H} are given by the expressions (26) or (32). The matrix equation (44) consists of the $(Pm + N)$

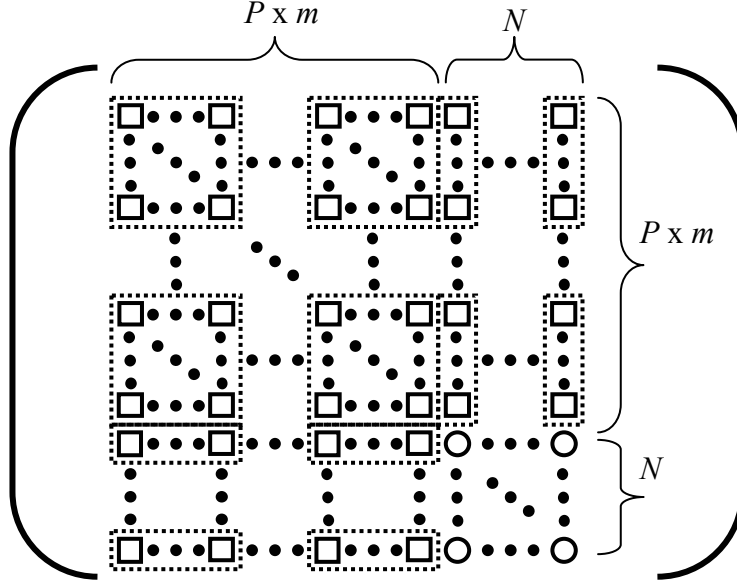


Fig. 11: Matrix reduction (multi port circuit)

scalar equations with the $(P + N)$ variables. Therefore, the matrices \mathbf{U} and \mathbf{H} should be reduced as is depicted in Fig. 11. The elements of matrix \mathbf{U} or \mathbf{H} bounded by the rectangles are added together, that way we obtain one element in reduced matrix \mathbf{U}_R or \mathbf{H}_R . The matrix equation (44) can be after reduction of matrices written as:

$$\mathbf{U}_R \cdot [V_{01} \ V_{02} \ \dots V_{oP} \ | \ V_1 \ V_2 \ \dots V_N]^T = \mathbf{H}_R \cdot \left[\frac{I_{01}}{m} \ \frac{I_{02}}{m} \ \dots \ \frac{I_{oP}}{m} \ | \ 0 \ 0 \ \dots 0 \right]^T. \quad (45)$$

Further step is a calculation of the impedance matrix \mathbf{Z} according to the equation (36). Reduced matrix equation (45) can be rewritten in extended form as follows:

$$\begin{bmatrix} V_{01} \\ \vdots \\ V_{0P} \\ V_1 \\ \vdots \\ V_N \end{bmatrix} = \begin{bmatrix} z_{1,1} & z_{1,2} & \dots & z_{1,P} & \dots & z_{1,P+N} \\ \vdots & \vdots & \vdots & \vdots & \vdots & \vdots \\ z_{P,1} & z_{P,2} & \dots & z_{P,P} & \dots & z_{P,P+N} \\ z_{P+1,1} & z_{P+1,2} & \dots & z_{P+1,P} & \dots & z_{P+1,P+N} \\ \vdots & \vdots & \vdots & \vdots & \vdots & \vdots \\ z_{P+N,1} & z_{P+N,2} & \dots & z_{P+N,P} & \dots & z_{P+N,P+N} \end{bmatrix} \cdot \begin{bmatrix} I_{01}/m \\ \vdots \\ I_{0P}/m \\ 0 \\ \vdots \\ 0 \end{bmatrix}. \quad (46)$$

The previous matrix equation gives the desired relations between the ports of the multi-port power bus structure:

$$\begin{bmatrix} V_{01} \\ V_{02} \\ \vdots \\ V_{0P} \end{bmatrix} = \begin{bmatrix} z_{1,1}/m & z_{1,2}/m & \dots & z_{1,P}/m \\ z_{2,1}/m & z_{2,2}/m & \dots & z_{2,P}/m \\ \vdots & \vdots & \ddots & \vdots \\ z_{P,1}/m & z_{P,2}/m & \dots & z_{P,P}/m \end{bmatrix} \cdot \begin{bmatrix} I_{01} \\ I_{02} \\ \vdots \\ I_{0P} \end{bmatrix}, \quad (47a)$$

The voltages at the sampling points around the periphery of the circuit can be evaluated from the matrix equation (46) as follows:

$$\begin{bmatrix} V_1 \\ V_2 \\ \vdots \\ V_N \end{bmatrix} = \begin{bmatrix} z_{P+1,1}/m & z_{P+1,2}/m & \cdots & z_{P+1,P}/m \\ z_{P+2,1}/m & z_{P+2,2}/m & \cdots & z_{P+2,P}/m \\ \vdots & \vdots & \ddots & \vdots \\ z_{P+N,1}/m & z_{P+N,2}/m & \cdots & z_{P+N,P}/m \end{bmatrix} \cdot \begin{bmatrix} I_{01} \\ I_{02} \\ \vdots \\ I_{0P} \end{bmatrix}. \quad (47b)$$

For practical reasons is important to know the voltage distribution between the plates of the power-bus structure. The proper choice of positions of critical ICs can eliminate structural resonances and radiated electromagnetic interferences. The voltage distribution

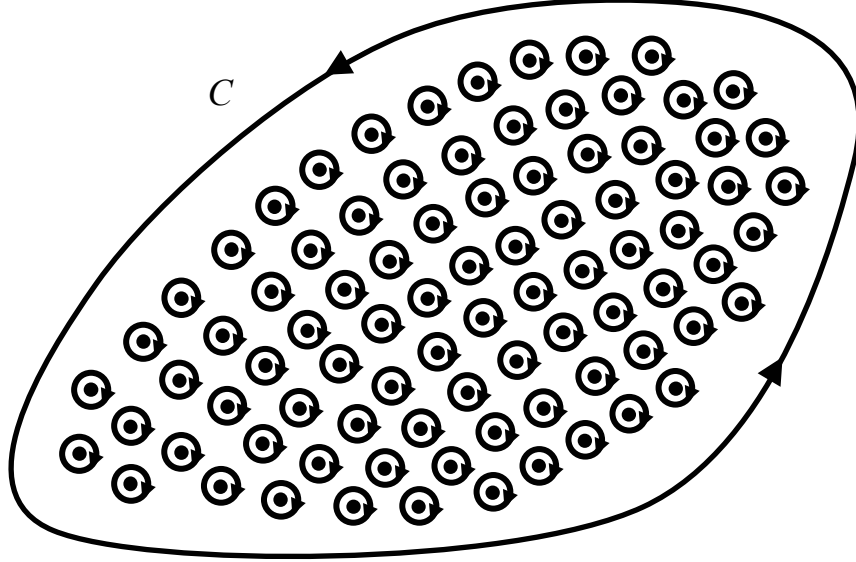


Fig. 12: *Evaluation of the voltage distribution between the plates of the parallel-plate structure*

between the plates of the parallel-plate structure can be computed according to the integral equation (21). The region between the plates of the structure is uniformly covered by the points, where contributions from the boundary are summed (see Fig. 12). These points must not lie at the boundary contour C . Then we specify the positions, where the structure will be excited by the current sources. The loops depicted in Fig. 12 are considered infinitesimally small and voltages at the centers of these loops are then given as:

$$\begin{bmatrix} V_{01} \\ V_{02} \\ \vdots \\ V_{0N} \end{bmatrix} = \frac{1}{2} \cdot \begin{bmatrix} \sum_i I_{0i} z_{1,i} \\ \sum_i I_{0i} z_{2,i} \\ \vdots \\ \sum_i I_{0i} z_{P,i} \end{bmatrix}. \quad (47c)$$

Here, index i denotes the position (x_i, y_i) , where the power-bus structure is excited. In this case, when the voltages are evaluated at singles points, parameter m is set to 1 and the lengths of corresponding segments approach to zero. The factor $1/2$ arises from the different half- and full-circuit extractions of the singularity described in section 2.4.

3.3 Computation of the Radiation Diagram

As was mentioned before, radiated electromagnetic interferences (EMI) are radiated as a consequence of switching noise and nonzero impedance of the power bus structure. These interferences can be suppressed by the proper design of the power-bus structure. The radiated fields at the structural resonances of a rectangular power-bus structure were analytically

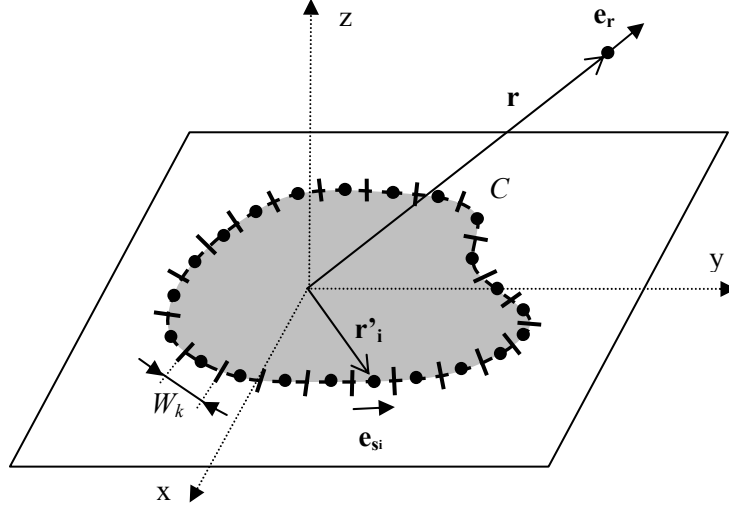


Fig. 13: Symbols used in the equation (50)

described in [1] using the field equivalence principle. At this chapter, we adopt the methodology from [1], to numerically compute the radiated fields of the power-bus structure with an arbitrary shape of power plate.

In the following text we suppose, that the lateral dielectric sides of the power-bus structure serve as the radiating apertures, where only tangential electric field E_z exists. This tangential aperture field is responsible for the radiated fields by the power-bus structure. According to the equivalence principle, the aperture tangential electric field E_z may be replaced by the equivalent magnetic surface current M_S located along the periphery of the power bus structure. As is described in [1], the voltage V between the plates of the parallel plate structure is given as:

$$V = M_S \cdot d = E_z \cdot d, \quad (48)$$

where d denotes the height of the substrate. Thus, the radiated far field can be computed using the equivalence principle as [1]:

$$\mathbf{E}(\mathbf{r}) = \frac{jk_0 d}{4\pi} \frac{e^{-jk_0 r}}{r} \int_C M_S(\mathbf{r}') e^{jk_0 \mathbf{r}' \cdot \mathbf{e}_r} (\mathbf{e}_r \times \mathbf{e}_s) ds, \quad (49)$$

where \mathbf{r} and \mathbf{r}' are the position vectors of the observation and source points, respectively. Next, the r denotes the distance of the observation point from the origin and \mathbf{e}_r , \mathbf{e}_s denote the unit vectors having the directions of the observation point from the origin and of the equivalent magnetic current along C , respectively.

The radiation integral (49) can be solved analytically only for the simple shapes of the parallel plate structure, e.g. for the rectangular power bus structure in [1]. For the arbitrarily shaped parallel plate structure, the integral (49) has to be solved numerically. Suppose that the

voltage evaluated at the i -th sampling point is constant along the i -th segment of the width W_i . Then the radiation integral can be rewritten as:

$$\mathbf{E}(\mathbf{r}) \approx \frac{jk_0 e^{-jk_0 r}}{4\pi r} \sum_{i=1}^N V(\mathbf{r}_i') e^{jk_0 \mathbf{r}_i' \cdot \mathbf{e}_r} (\mathbf{e}_r \times \mathbf{e}_{s_i}) W_i, \quad (50)$$

where $V(\mathbf{r}_i')$ denotes the voltage at the i -th sampling point and W_i is the width of the i -th element (see Fig. 13).

The analyzed power bus structure is surrounded by a sphere, where the observation points are placed. After evaluation of expression (50) at each observation point, the magnitude of computed electric intensity can be plotted as 3D radiation diagram.

3.4 Implementation and the Program Structure

The described contour integral method was implemented in Matlab. The program is compound of several m-files. In the main m-file, the following input parameters of an analysis can be entered:

- Frequency range and frequency step of an analysis
- Coordinates of an M -polygon
- Substrate parameters (height, relative permittivity, dielectric loss tangent) and conductivity of the plates
- Number of ports, radius of the ports and coordinates of the ports

After entering input data, the main m-file executes the calculation of coordinates of the segments and of the sampling points on the contour C . The number of the segments is

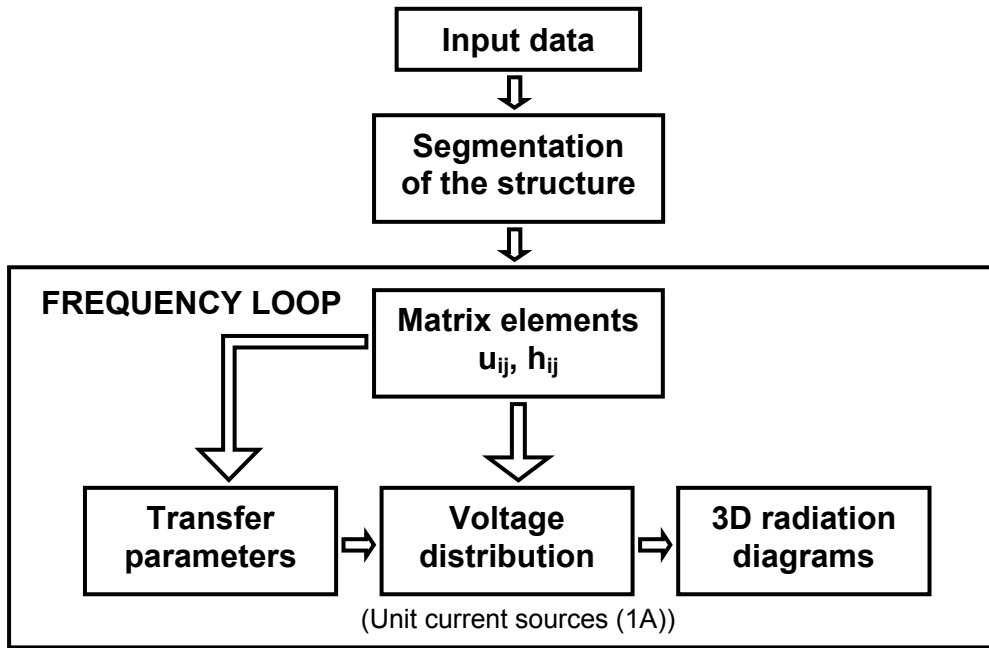


Fig. 14: *Structure of the program*

calculated according to minimum wavelength λ_{min} in the dielectric layer. The maximum width of the segment along the periphery is implicitly set to $0.1 \lambda_{min}$. The value of the multiple of λ_{min} can be also set manually. The structure is excited by the unit current sources $I_{0k} = 1A$. The radius of the ports should be much less than the wavelength in the dielectric layer and the shortest distance of the ports to the sampling points along the periphery should be much

longer than the radius of the ports. The simple graphical user interface of the Matlab program is depicted in Fig. 39 (Appendix). Note that the checkboxes for the voltage distribution and 3D radiation diagram are active only if the start and stop frequencies are equal.

The second part of the program is the frequency loop. In this loop, the matrix coefficients and transfer parameters are calculated. It is possible to choose the way of computing of the matrix elements after equations (26) or (32). The integration in (32) is implemented using the Gauss-Legendre method. Further, the frequency loop contains the m-file, which executes the matrix reductions and the part of the evaluation of the voltages along the periphery of the circuit. The voltages at the sampling points along the periphery are the input data for the calculation of the 3D radiation diagrams. The transfer parameters, voltages or the radiation diagrams can be subsequently displayed. The structure of the program is shown in Fig. 14.

3.5 Circuit Level Simulation

A further step in the analysis of the power-bus structures is the inclusion of lumped elements connected to the ports of the structure. Mainly we are interested in the behavior of the structure with decoupling capacitors. Decoupling capacitors are connected between the power and ground planes to reduce the high-frequency impedance. These capacitors usually exhibit capacitance values about a few tens of nano-Farads and the parasitic inductance and resistance represented by the equivalence series inductance (ESL) and by the equivalence series resistance (ESR), respectively.

In the previous sections, we have shown how to compute the voltage/current relations between the ports of the arbitrarily shaped N-port structure. These relations in the form of Z-matrix will be used to simulation of the power-bus structures populated by the lumped elements.

At first, the Z-matrix of an analyzed structure is computed in Matlab and saved as the data *.mat file. This data file is consequently in Matlab converted into the standardized *Touchstone format*², which is compatible for the most of CAD circuit analyzing programs. In the last step, the N-port model of the structure is, in the appropriate computer circuit analyzer, used to simulate the populated power-bus structure.

4 Results

The techniques described above, are first validated by the simulation of the simple rectangular power-bus structure described using analytical expressions. The analysis of a polygonal structure is verified by a commercial 3D full-wave solver.

4.1 One-Port Rectangular Power-Bus Structure

The input impedance of a power bus structure, the voltage distribution between the plates and 3-D radiation diagrams can be compared with the analytical results from [1]. In the case of a rectangular power-bus structure, Green's function for the Helmholtz equation (5)

² A Touchstone® file (also known as an SnP file) is an ASCII text file used for documenting the n-port network parameter data of an active device or passive interconnect network. While Touchstone files have been accepted as a de-facto standard for the transfer of frequency dependent n-port network data [6].

can be expanded into the complete set of the familiar trigonometric eigenfunctions, thus we get [1]:

$$\frac{V(x, y)}{I_0(x_0, y_0)} = \frac{j\omega\mu_0 d}{WL} \sum_{m=0}^{\infty} \sum_{n=0}^{\infty} K_{m,n} \frac{\cos(k_{xm}x_0) \cos(k_{yn}y_0)}{k_{xm}^2 + k_{yn}^2 - k^2} \cos(k_{xm}x) \cos(k_{yn}y), \quad (51)$$

where W and L denote the width and length of the rectangular power-bus structure and the discrete wave numbers are given as:

$$k_{xm} = \frac{m\pi}{L}, \quad k_{yn} = \frac{n\pi}{W},$$

The normalizing constant K_{mn} is defined as:

$$K_{mn} = \begin{cases} 1, & \text{for } m = n = 0 \\ 2, & \text{for } m = 0 \vee n = 0 \\ 4, & \text{for } m \neq 0 \wedge n \neq 0 \end{cases}$$

For the computation of the input impedance, the finite size of port has to be taken into account. Therefore the equation (51) is multiplied by the sinc factors and the transfer impedance between the ports at the positions (x, y) and (x_0, y_0) is given as [7]:

$$\begin{aligned} Z(x, y | x_0, y_0) &= \frac{j\omega\mu_0 d}{WL} \sum_{m=0}^{\infty} \sum_{n=0}^{\infty} \frac{K_{m,n}}{k_{xm}^2 + k_{yn}^2 - k^2} \\ &\times \cos(k_{xm}x) \cos(k_{yn}y) \cos(k_{xm}x_0) \cos(k_{yn}y_0) \\ &\times \text{sinc}(k_{xm}d_x/2) \text{sinc}(k_{yn}d_y/2) \text{sinc}(k_{xm}d_{x0}/2) \text{sinc}(k_{yn}d_{y0}/2) \end{aligned}, \quad (52)$$

where d_x, d_{x0}, d_y, d_{y0} are the dimensions of the rectangular ports. Since the real ports have the circular cross-section, the equivalent radius is considered [8]:

$$r_e = 0.59a,$$

where $a = d_x = d_{x0} = d_y = d_{y0}$.

Fig. 15 shows the analyzed one-port rectangular power bus structure with the dimensions $L = 300$ mm and $W = 200$ mm is depicted in Fig. 15. The port with radius $r = 1$ mm was placed at the position $(x_0, y_0) = (50, 50)$ mm. At this position, the structure is excited by the unit current source, which represents the noise source. The analysis was carried out at the range of frequencies $f = (10 \div 1000)$ MHz with the frequency step 5 MHz. The maximum length of segments was $0.1 \lambda_{min}$. The height of the substrate is $d = 1.5748$ mm (62 mils), relative permittivity is $\epsilon_r = 4.35$, dielectric loss tangent is set to $\tan \delta = 0.02$ and conductivity of the plates is $\sigma = 5.8 \cdot 10^7$ S/m. The same parameters of the substrate and the geometry of the ports are considered throughout the chapter 4.

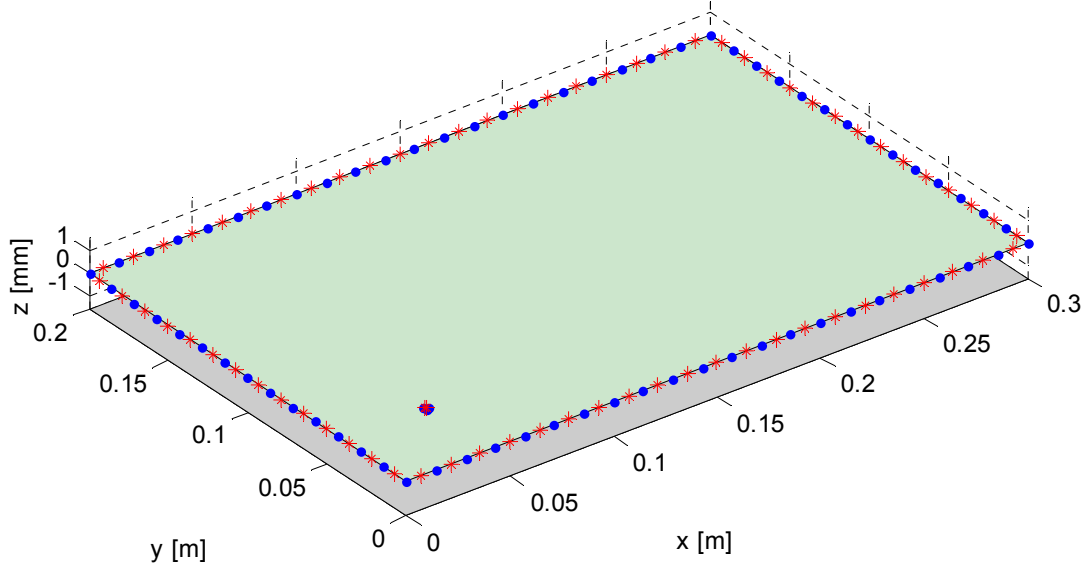


Fig. 15: Analyzed one-port rectangular power-bus structure

Fig. 16 shows the calculated magnitude of the input impedance $Z_{inp} = |V(x_0, y_0)/I_0(x_0, y_0)|$ using the analytical expression (52), our program in Matlab and ANSOFT Designer. The matrix elements u_{ij} and h_{ij} were computed using the simple expressions (26)

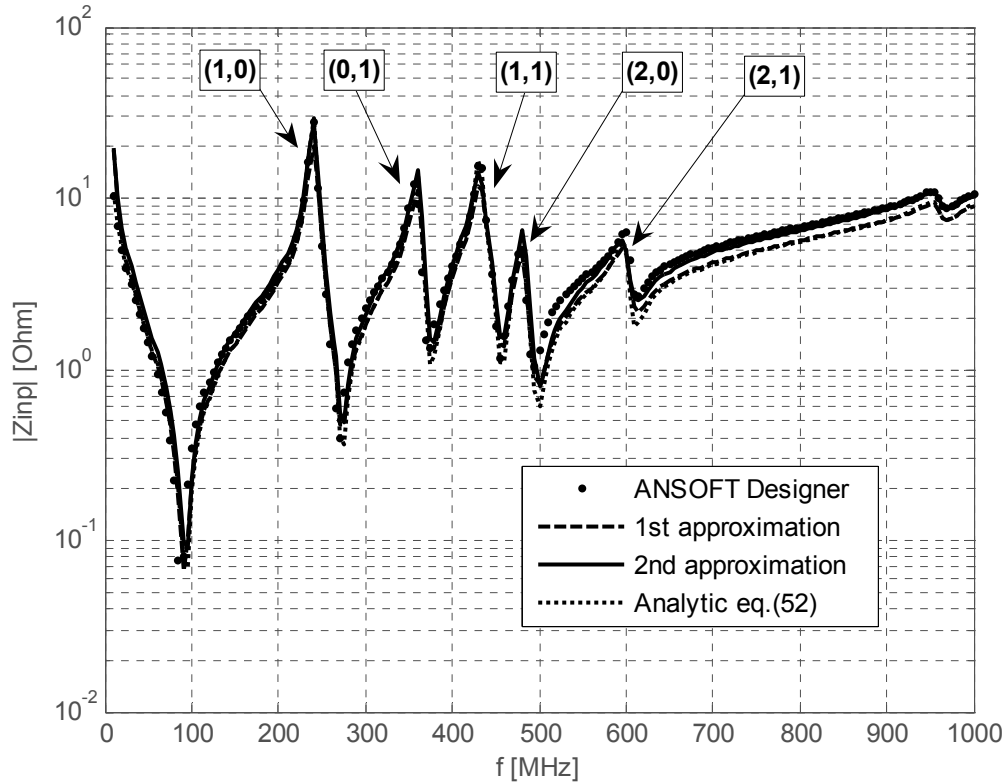


Fig. 16: Absolute value of the input impedance of an analyzed rectangular power-bus structure

denoted as the 1st approximation and using the expressions (32) denoted as the 2nd approximation. In the analytical expression (52) 1000 terms were considered in each of the sums. The model of the structure in ANSOFT Designer was covered by the 631 triangles. As can be seen, the analytical and the numerical results are in good agreement. Further, the first

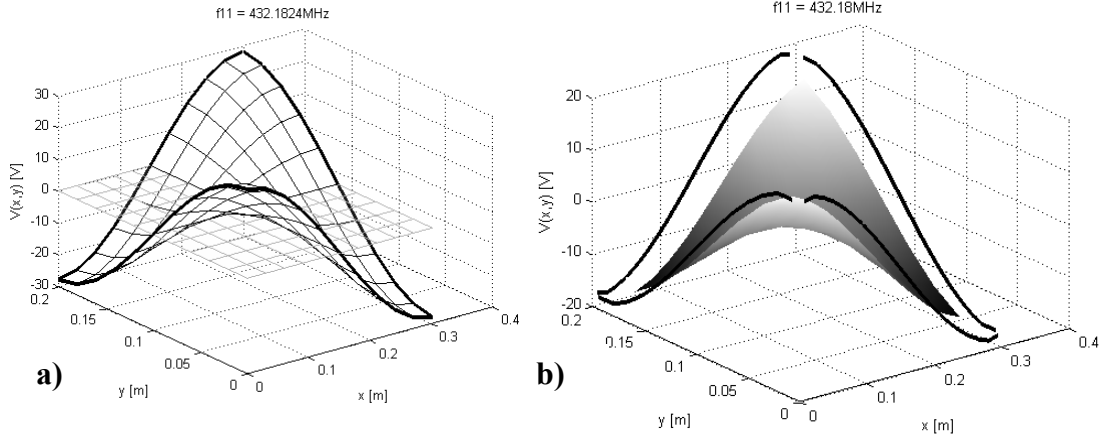


Fig. 17: Voltage distribution $V(x,y)$ for the resonant mode $(1,1)$.
a) Analytically computed, b) numerically computed

five structural resonances are labeled in Fig. 16. Maximum differences between the analytical and numerical results (2nd approximation and ANSOFT Designer) appear at the frequencies higher than 500 MHz.

In Fig. 17 are depicted voltage distributions $V(x,y)$ between the plates of the rectangular power-bus structure at the resonant frequency $f_{1,1}$. The voltage distribution in the

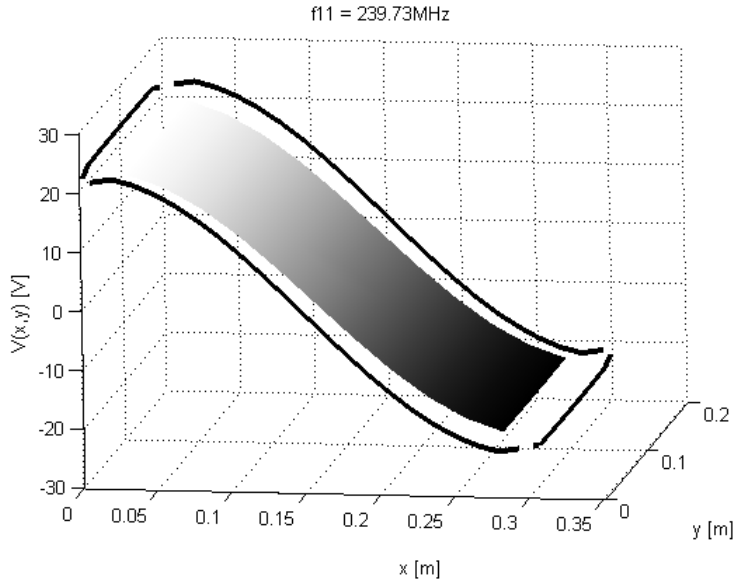


Fig. 18: Voltage distribution for the first resonant mode $(1,0)$

first figure from the left was computed according to analytical expression (51). The second figure shows the numerically computed voltage distribution between the plates and at the sampling points along the periphery of the structure.

Fig. 18 shows numerically computed voltage distribution $V(x,y)$ of the first resonant frequency $f_{1,0}$. The lowest resonant mode is usually operating mode for the microstrip antennas. In Fig. 19 are depicted 3D radiation diagrams of power-bus structure at the $f_{1,0}$. The

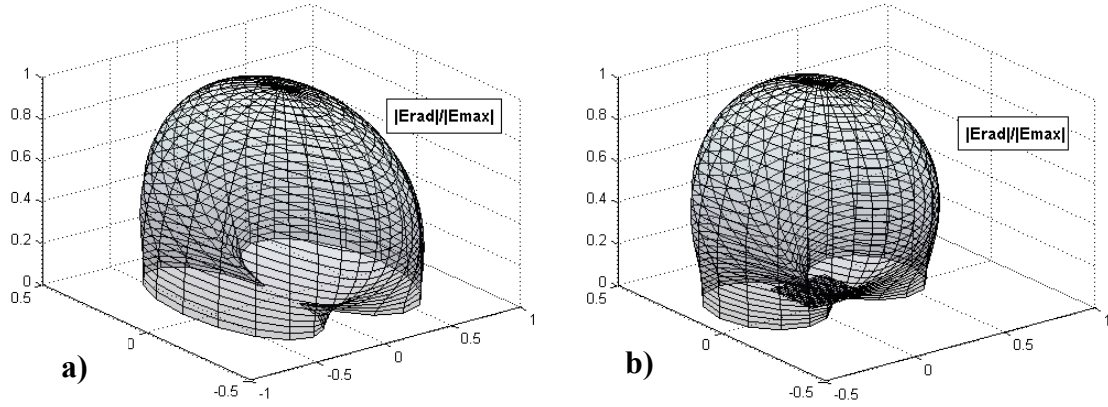


Fig. 19: 3D radiation diagrams for the resonant mode (1,0).
a) analytically computed, b) numerically computed

first one from the left was computing using the analytical expression introduced in [1]. This expression is obtained after integration of a radiation integral (49) along the rectangle, with using the field equivalence principle. The radiation diagram in Fig. 19b was obtained from the voltages along the periphery of the structure (see Fig. 18) using the expression (50). The differences are especially due to the errors in computing of the voltage distribution and due to the presumptions for the validity of expression (50).

In this section we have computed the input impedance, voltage distributions and the 3D radiation diagrams for the simple rectangular power-bus structure. The presented numerical approach was verified using existing analytical expressions.

4.2 One-Port Arbitrarily Shaped Power-Bus Structure

As an example for an arbitrarily shaped power-bus structure, the geometry shown in Fig. 20 was chosen. The substrate has the same parameters as in the previous section. The structure is excited at the position $(x_0, y_0) = (100 \text{ mm}, 100 \text{ mm})$. Because of the complicated

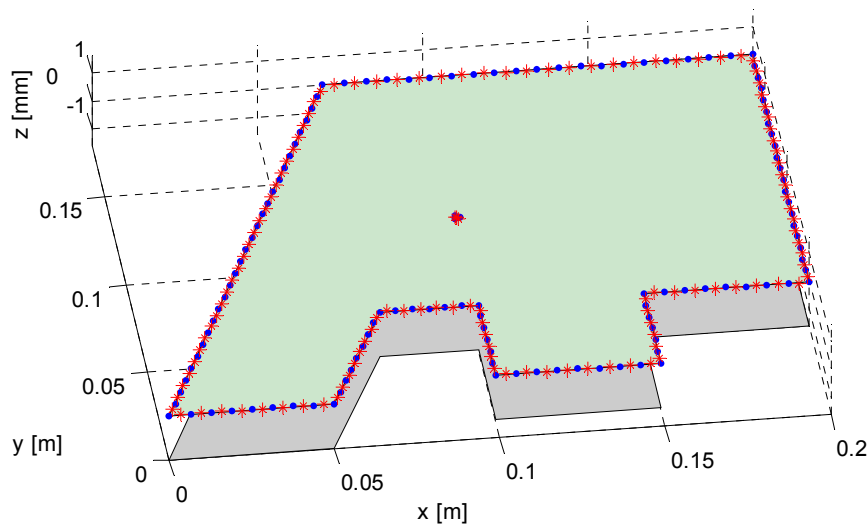


Fig. 20: Analyzed one-port polygonal shaped power-bus structure

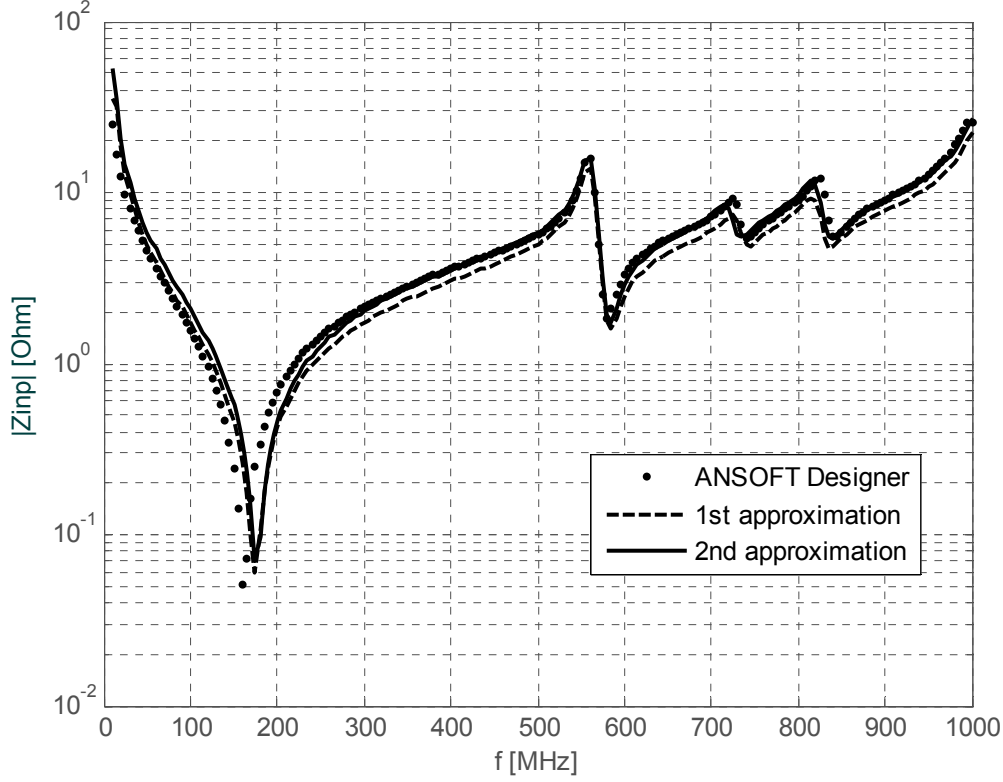


Fig. 21: *Absolute value of the input impedance of an analyzed arbitrary shaped power-bus structure*

shape of the structure, we have increased the number of the segments by setting the condition $W_{max} = 0.05 \lambda_{min}$, where W_{max} denotes the maximum width of the segments, considering the non-uniform segmentation of an arbitrarily shaped structure.

Fig. 21 shows the computed magnitude of the input impedance using the ANSOFT Designer and our program in Matlab. The matrix elements u_{ij} and h_{ij} were computed according to the first and the second approximations (26) and (32), respectively. The mesh in

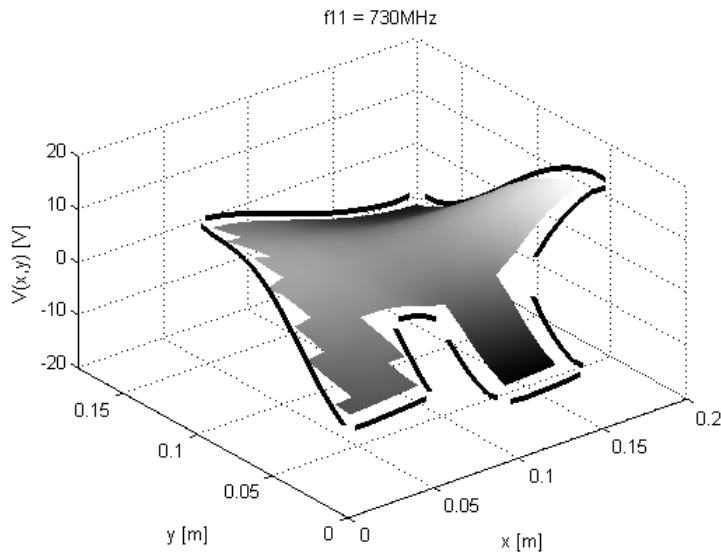


Fig. 22: *Voltage distribution at the second resonance frequency*

ANSOFT Designer included 310 triangles. As can be seen, the computed input impedance is in good agreement with the results from ANSOFT Designer.

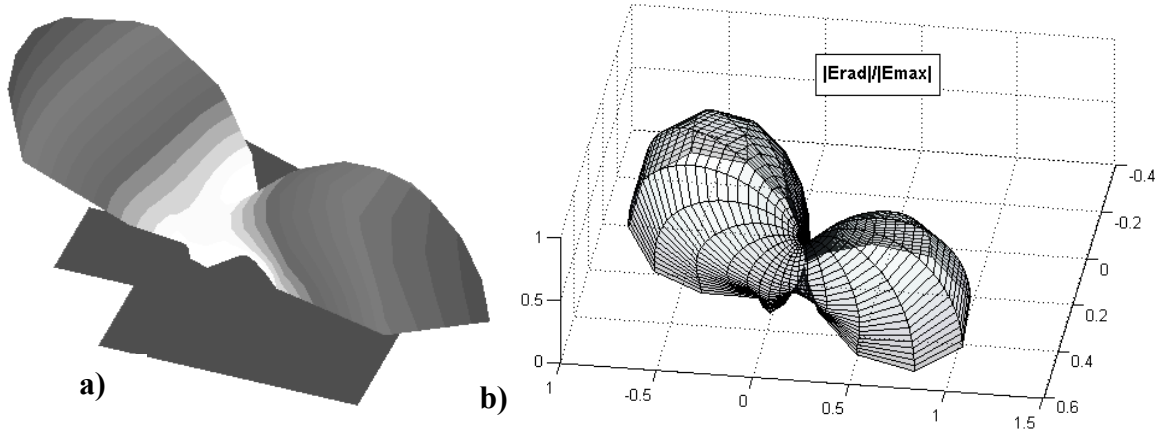


Fig. 23: 3D radiation diagrams at the second resonance frequency.
a) ANSOFT Designer, b) Matlab

Fig. 22 shows the voltage distribution $V(x,y)$ between the plates of the power-bus structure depicted in Fig. 20. The voltage distribution was computed at the second resonance frequency $f = 730$ MHz. The radiation diagrams depicted in Fig. 23a and in Fig. 23b were computed at the same frequency in ANSOFT Designer and in Matlab, respectively. In both diagrams are apparent the two bold side-lobes.

The structural resonances can be effectively eliminated by a proper placement of the critical ICs [1]. This fact can be illustrated in Fig. 24 and Fig. 25. Fig. 24 shows the voltage distributions $V(x,y)$ for three different positions of the ports: $(x_{p1}, y_{p1}) = (50, 50)$ mm, $(x_{p2}, y_{p2}) = (100, 100)$ mm and $(x_{p3}, y_{p3}) = (180, 160)$ mm and in Fig. 25 are depicted the magnitudes of the input impedances for these different positions. Analyses were carried out at the frequency range $(10 \div 1000)$ MHz with the step 10 MHz.

As can be seen from Fig. 25, at the first and at the third position of the port, the input impedance steeply increases around the frequency $f = 340$ MHz. This is the first mode resonance frequency. The corresponding voltage distributions are depicted in Fig. 24b and Fig. 24c. In contrast to these cases, the input impedance for the second position of the port, in the center of the power plate, exhibits no resonance at this frequency. The corresponding magnitude of the voltage distribution between the plates is depicted in Fig. 24c. Since the structure is not in resonance at this frequency, the magnitude of the voltage between the plates is much lower compared to the first and the second cases. The first resonance at this point occurs around $f = 560$ MHz.

In conclusion, the excitation of the structural resonances strongly depends on the position of the port. At an analyzed range of frequencies, the port at the first position excites the three structural resonances and the ports at the second and the third positions excite two and five structural resonances, respectively. In general, the ports near the corners of the PCB excite more resonances than the ports placed in the middle of the power planes.

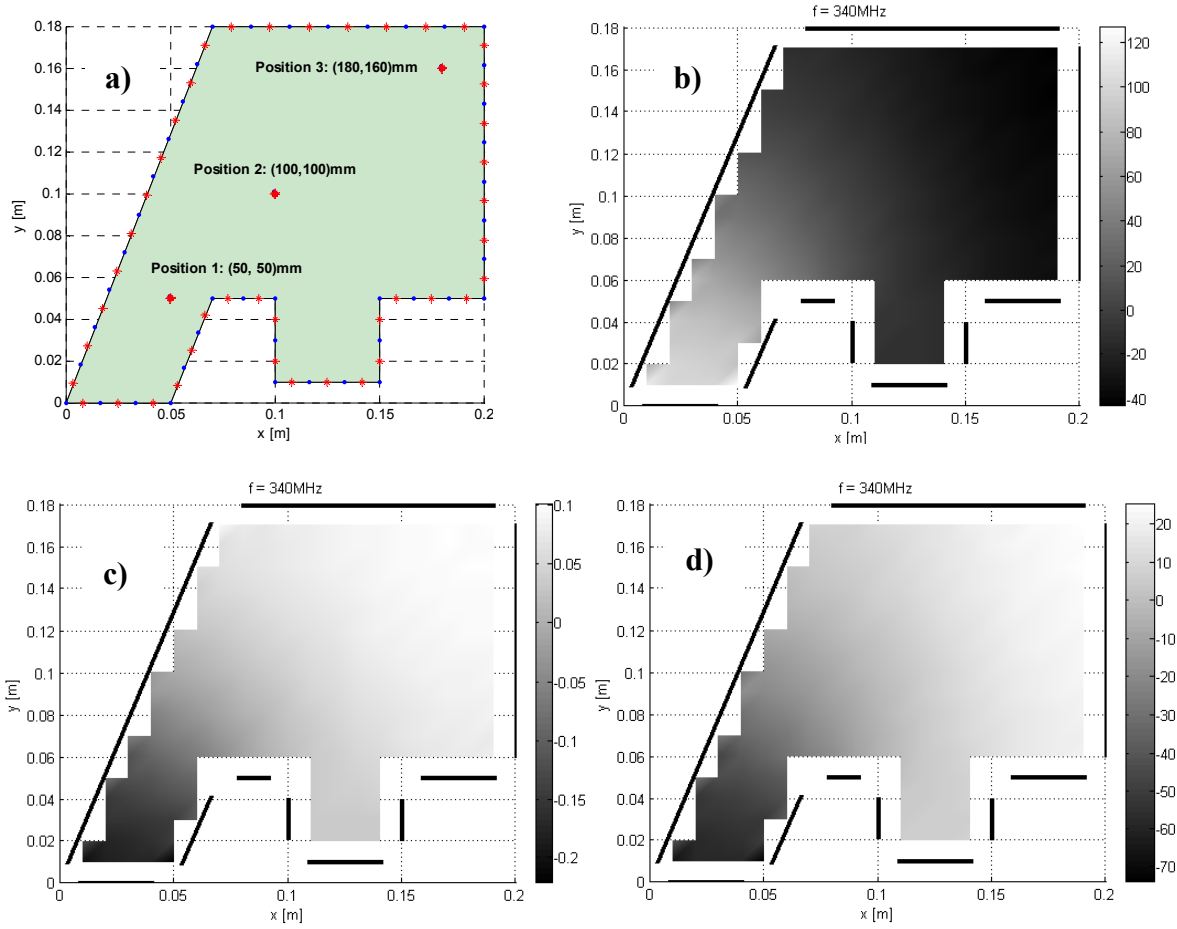


Fig. 24: Voltage distributions at $f = 340 \text{ MHz}$ for different positions of the ports. *a)* Positions of the ports, *b)* Position 1: (50, 50) mm, *c)* Position 2: (100, 100) mm, *d)* Position 3: (180, 160) mm

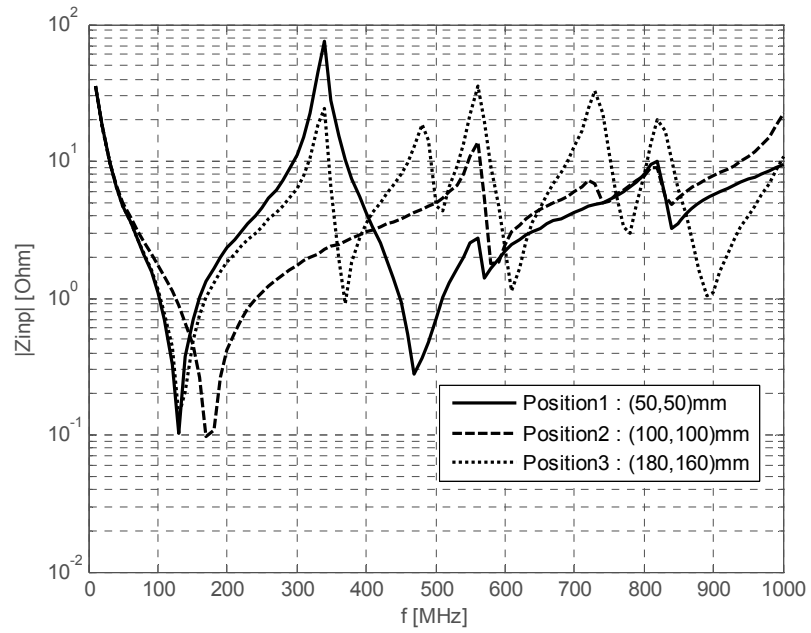


Fig. 25: Absolute value of the input impedance for the different port positions

4.3 Accuracy and Computational Demands of the Implemented Algorithm

In this section, the simple rectangular power-bus structure depicted in Fig. 15 is analyzed to obtain the information about the accuracy and computational demands of implemented algorithm. As a reference, the truncated analytical expression (52) with 1000 terms in each of sums is considered. All analyses were performed with a 1.6-GHz CPU and 512-MB memory.

Analyses were carried out for the three ratios $\lambda_{min}/W_{max} = \{5, 10, 20\}$ at the frequency range $(10 \div 1000)$ MHz with a frequency step 5 MHz. The port of radius $r = 1$ mm had 4 segments around the periphery. The input impedances $|Z_{inp}|$ computed by the first approximations (26) and the second approximations (32) are depicted in Fig. 26a and Fig. 26b, respectively. As can be seen, the maximum errors occur at the resonance frequencies. Obviously, the errors decrease when the number of elements increases or alternatively, the ratio λ_{min}/W_{max} increases. For determination of a total error over the frequency range, the

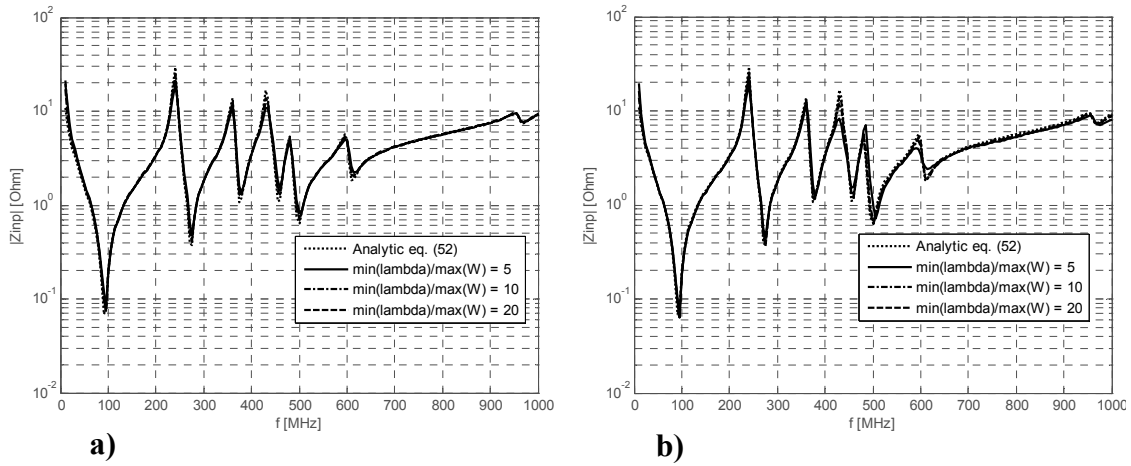


Fig. 26: Input impedance $|Z_{inp}|$. a) 1st approximation, b) 2nd approximation

mean square error (MSE) was computed. The calculated mean square errors in dependence on the ratio λ_{min}/W_{max} and the integration method are listed in Tab.1. We can observe, that the second approximations (32) gives in terms of MSE, except the first case, more accurate results then the first approximations (26). However, the application of the second approximations is more time consuming. From given results we can state, that the CIM algorithm is not very much sensitive with respect to the change of λ_{min}/W_{max} ratio. A satisfactory insight in the behavior of the structure can be obtained already with only 5 segments per minimum wavelength. Since the maximum length of the segment W_{max} is related to the minimum wavelength in the dielectric layer λ_{min} , we can expect better simulation results accuracy at low frequencies, where the relative segment length W/λ is small.

A high efficiency of the boundary element methods consists in the dimension reduction of the problem. Consequently, the mesh of the numerical model is simpler and the

Tab. 1: Mean square errors

method	1st approximation			2nd approximation		
λ_{min}/W_{max} [-]	5	10	20	5	10	20
N [elements]	33	61	117	33	61	117
MSE [Ω^2]	1.6138	1.1143	0.4406	2.0799	0.66792	0.2483

implementation of these methods is easier. In Fig. 27 is depicted the number of discretization elements in dependence on the ratio λ_{min}/l_{max} for the 2D mesh in ANSOFT Designer and for the 1D mesh in our Matlab program. We can observe the linear and quadratic dependence of the number of elements on the ratio λ_{min}/l_{max} for the 1D and 2D mesh, respectively.

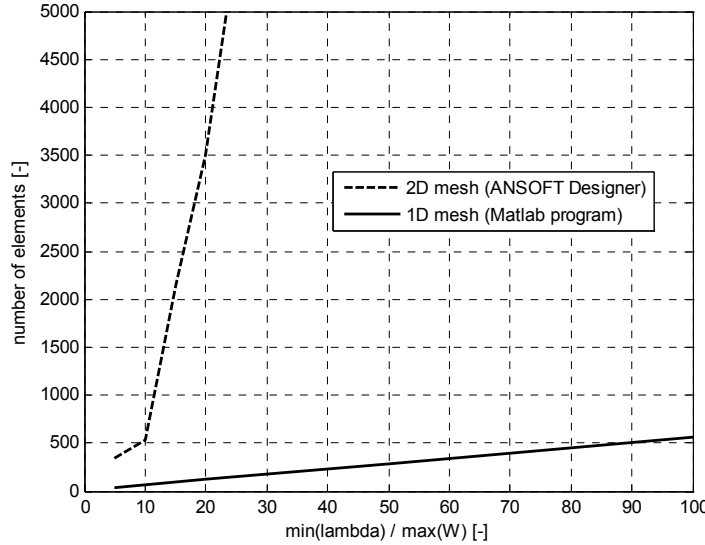


Fig. 27: Number of the discretization elements in dependence on the ratio l_{max}/λ_{min}

Obviously, the number of the discretization elements is directly related to the number of unknowns in the resulting system of linear equations. Considering, for example, the common Gauss elimination method, which for solving the N linear equations requires approximately $(N^3/3)$ of arithmetic operations. Then the computational demands of the boundary element methods are, for the fixed ratio λ_{min}/l_{max} , 3 exponent orders lower. Another reduction of the computational demands is usually achieved using the symmetry of the impedance matrix \mathbf{Z} . This reduction cannot be used in the presented numerical approach, since the impedance matrix is unsymmetrical, because of the angle θ_{ij} , which is not, in general, equal to θ_{ji} (see Fig. 8).

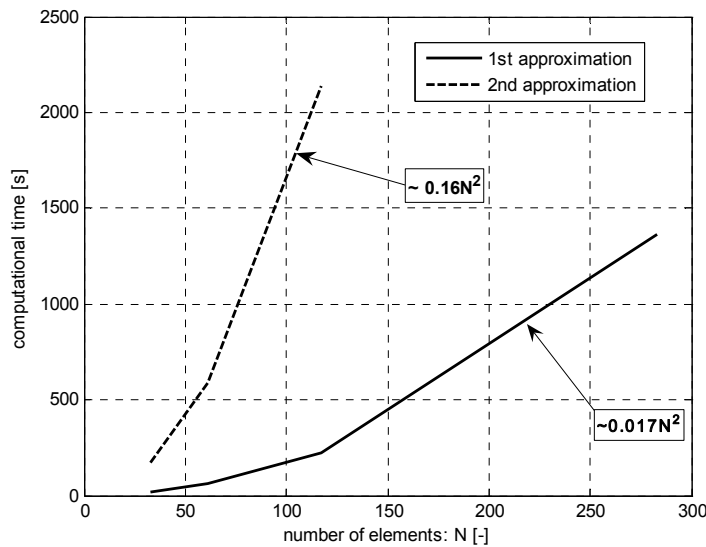


Fig. 28: Computational time in dependence on the number of elements

Fig. 28 shows the computational times of an aforementioned CIM analysis of the rectangular power-bus structure depending on the number of discretization elements. As can be seen, the computational times of both analyses using the first and second approximate expressions increase with the $O(N^2)$. This dependence is steeper for the second approximations (32). If the system of linear algebraic equations is solved using the common Gauss elimination, we can expect $O(N^3)$ dependence for high N . The choice between the first and the second approximations should be made with regard to accuracy and computational demands.

4.4 Matlab Program vs. ANSOFT Designer

Since ANSOFT Designer is based on the 3D full-wave method of moments (MoM) and our program uses the 2D contour integral method (CIM), it is not possible to set the same input parameters for the exact comparison of both approaches. However, the methods can be compared when we set the same maximum lengths of the discretization elements. In case of the MoM we set the maximum length of the sides of the triangles and in case of CIM we set the same rule for the maximum length of the boundary segments. The maximum length of the discretization elements is based on the minimum wavelength in the dielectric layer.

The simple one-port rectangular power-bus structure of the dimensions (300mm x 200 mm) was chosen as a benchmark sample. For a comparison of the results from both programs, the following ratios were used:

$$\frac{\lambda_{\min}}{l_{\max}} = \{5, 7, 10\},$$

where l_{\max} denotes the maximum length of the discretization element and λ_{\min} is the minimum wavelength in the dielectric layer. The position of the excitation port is $(x_0, y_0) = (50, 50)$ mm and the parameters of the substrate are the same as in the previous sections. All computations in this section were carried out for the range (20÷800) MHz with the step 10 MHz.

The geometry of the first tested structure for the ratio $\lambda_{\min}/l_{\max} = 10$ is depicted in Fig. 29. The structure was discretized into 61 boundary elements and 997 triangles in Matlab

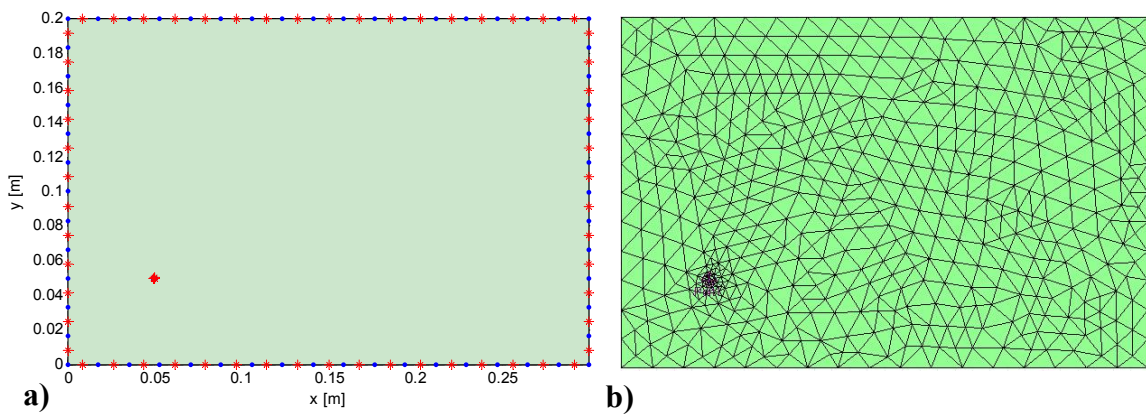


Fig. 29: Geometry of an analyzed power-bus structure for $\lambda_{\min}/l_{\max} = 10$
a) Matlab b) ANSOFT Designer

and in ANSOFT Designer, respectively. For the calculation of the matrix elements u_{ij} and h_{ij} in Matlab, the first approximations (26) and the second approximations (32) were used. Fig. 30 shows the computed absolute value of the input impedance versus frequency. As can be seen,

the results computed in Matlab and in ANSOFT Designer are almost identical. Obvious differences between the 1st approximation results from Matlab and results from ANSOFT

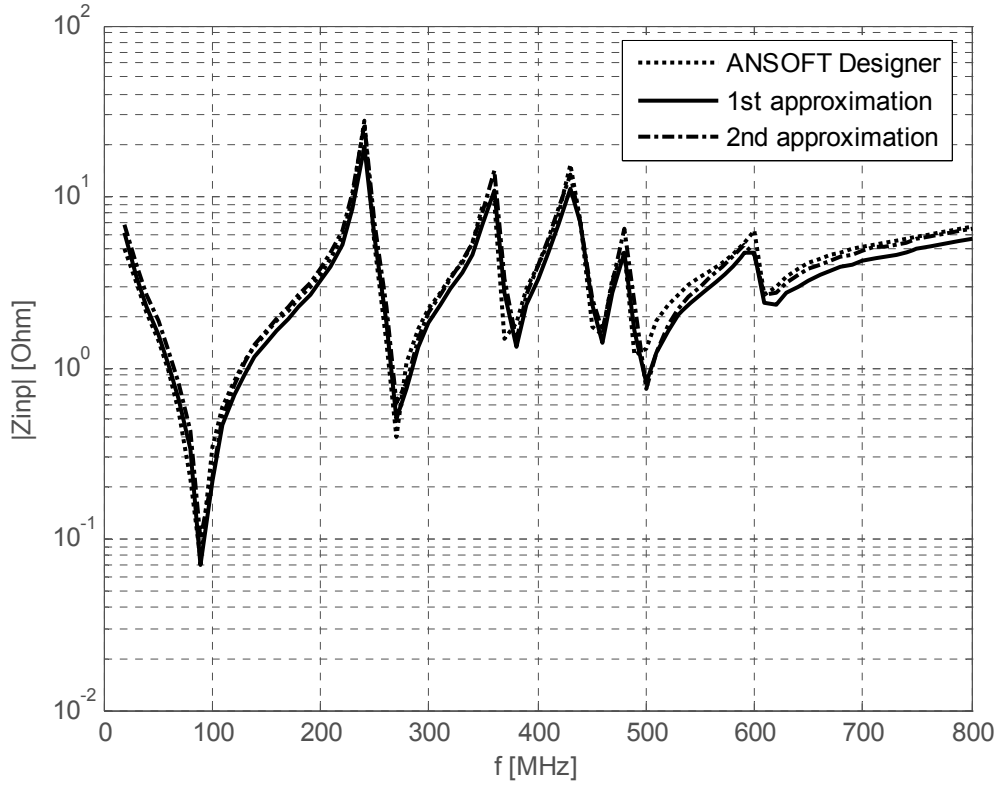


Fig. 30: Absolute value of the input impedance of the tested structure for $\lambda_{min}/l_{max} = 10$

Designer occur only at higher frequencies. In Tab. 2 are summarized all computational parameters of the Matlab and ANSOFT Designer simulation. The analysis using our program in Matlab is much less time consuming.

Tab. 2: Parameters of analyses for $\lambda_{min}/l_{max} = 10$

$\lambda_{min}/l_{max} = 10$ (79 frequency steps)			
Program	MATLAB		ANSOFT Designer
	1st appr.	2nd appr.	
Number of Elements	61 elements		997 triangles
Computational Time [h:mm:ss]	0:01:04	0:10:00	0:41:07

Further we have executed the same analyses for the smaller ratios λ_{min}/l_{max} . The conclusions of these analyses are similar to the previous one. Again, differences between the results computed using Matlab program and ANSOFT Designer are apparent only at the higher frequencies. The computational time of our Matlab program is much shorter than the computational time of ANSOFT Designer. The geometries and input impedances of analyzed structures for different ratios λ_{min}/l_{max} are shown in the following figures. The computational times and the numbers of discretization elements are summarized in the Tab. 3 and Tab. 4.

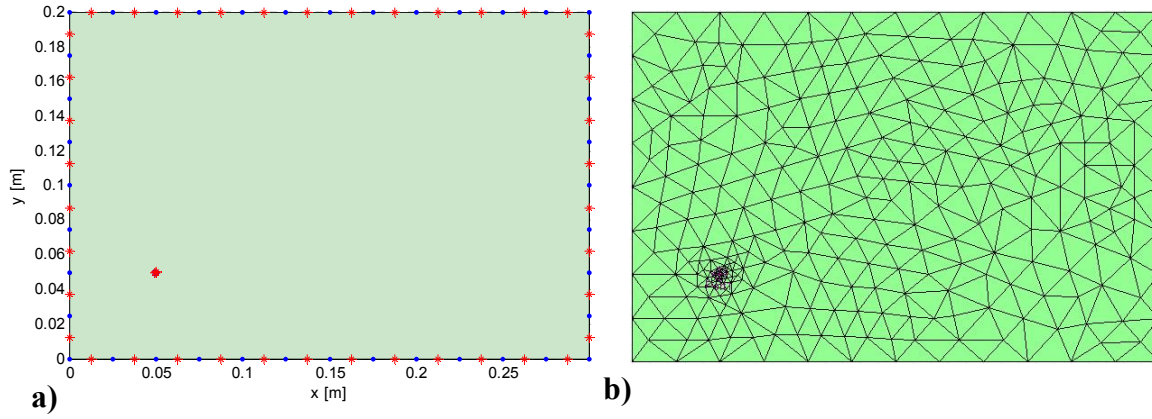


Fig. 31: Geometry of an analyzed power-bus structure for $\lambda_{\min}/l_{\max} = 7$
a) Matlab b) ANSOFT Designer

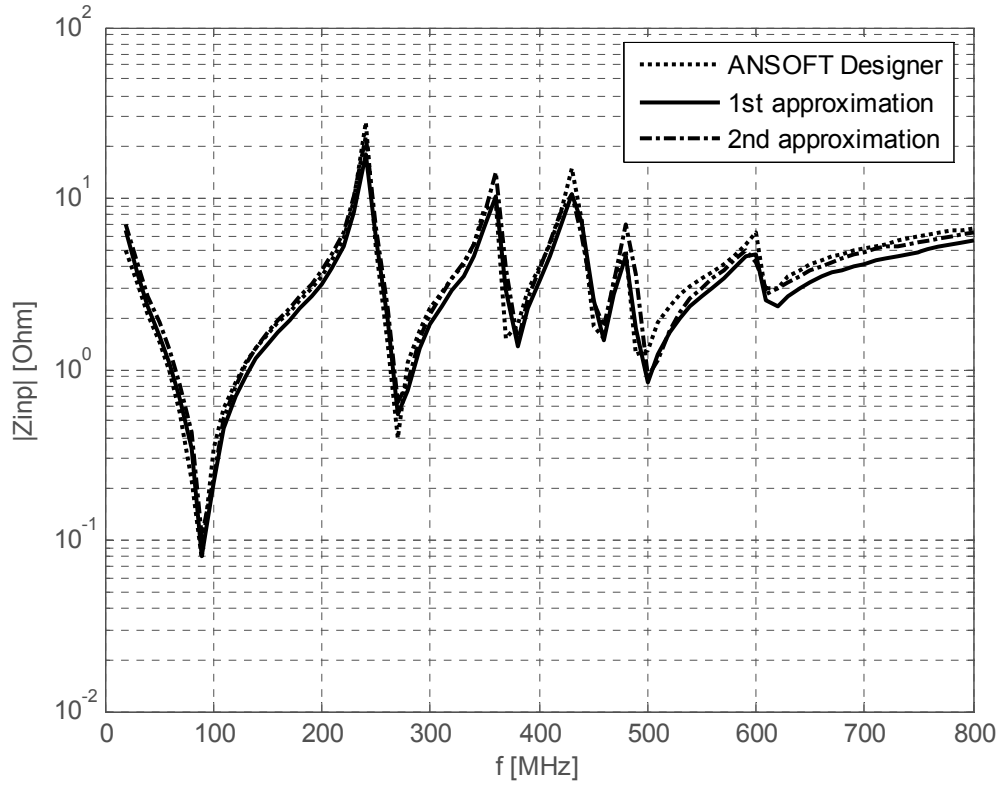


Fig. 32: Absolute value of the input impedance of the tested structure for $\lambda_{\min}/l_{\max} = 7$

Tab. 3: Parameters of analyses for $\lambda_{\min}/l_{\max} = 7$

$\lambda_{\min}/l_{\max} = 7$ (79 frequency steps)			
Program	MATLAB		ANSOFT Designer
	1st appr.	2nd appr.	
Number of Elements	43 elements		565 triangles
Computational Time [h:mm:ss]	0:00:31	0:04:58	0:12:32

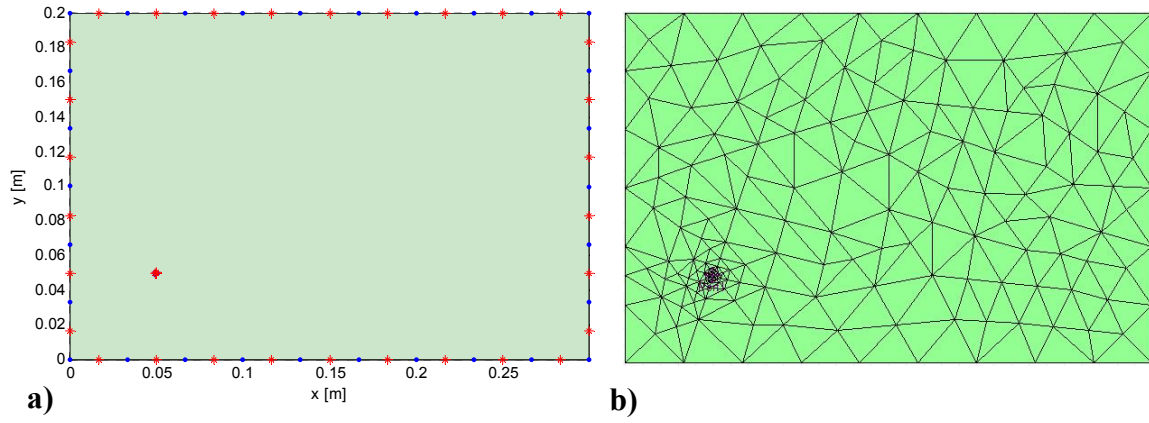


Fig. 33: Geometry of an analyzed power-bus structure for $\lambda_{min}/l_{max} = 5$.
a) Matlab b) ANSOFT Designer

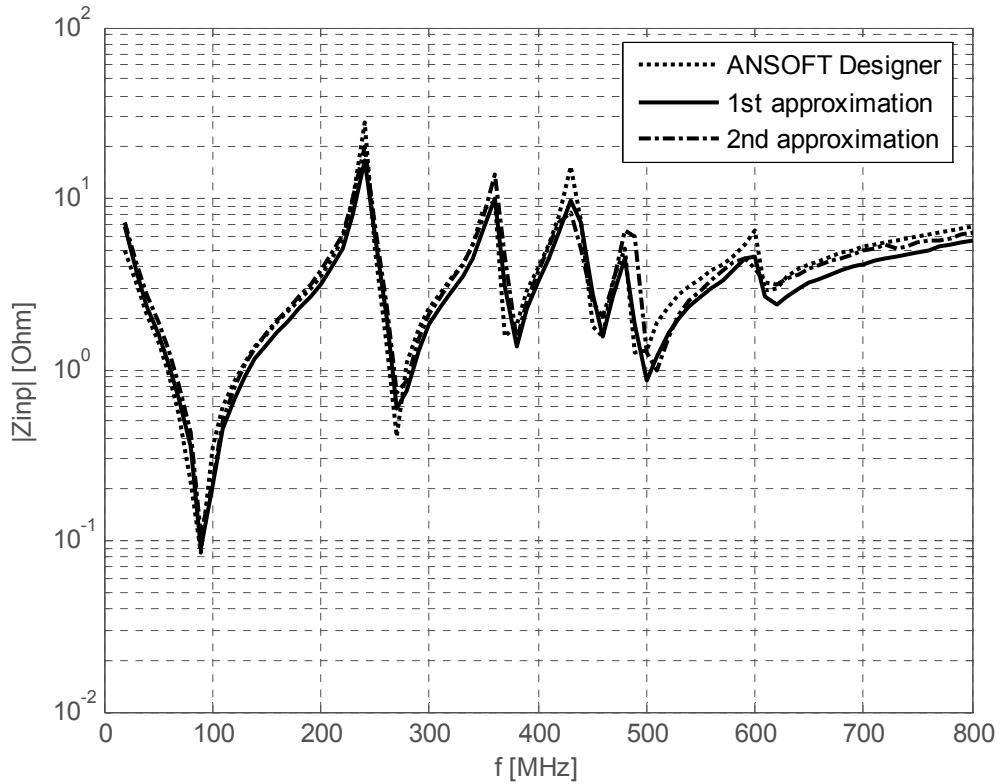


Fig. 34: Absolute value of the input impedance of the tested structure for $\lambda_{min}/l_{max} = 5$

Tab. 4: Parameters of analyses for $\lambda_{min}/l_{max} = 5$

$\lambda_{min}/l_{max} = 5$ (79 frequency steps)			
Program	MATLAB		ANSOFT Designer
	1st appr.	2nd appr.	
Number of Elements	33 elements		346 triangles
Computational Time [h:mm:ss]	0:00:19	0:02:56	0:06:12

5 Experimental Validation

The first tested power-bus structure was simple rectangular of the dimensions (160 mm x 100 mm) with the one port at the position (20, 80) mm. The test port was constructed using a SMA connector soldered to the PCB. The substrate was FR4 with a relative permittivity of $\epsilon_r = 4.2$, dissipation factor of $\tan\delta = 0.02$ and thickness of $d = 1.6$ mm. The input impedance was measured with the R&S ZVL (9 kHz to 6 GHz) network analyzer.

In the simulations, the SMA connector was modeled using a simple LC model of the transmission line. Corresponding values of the capacity and inductance were computed according to the expressions derived for a coaxial cable [12]:

$$C = \frac{2\pi\epsilon_0\epsilon_r l}{\ln \frac{r_2}{r_1}} \approx 725 \text{ fF} \quad \text{and} \quad L = \frac{\mu_0}{2\pi} l \ln \frac{r_2}{r_1} \approx 1.9 \text{ nH} ,$$

where $l = 7.5$ mm is the length of the modeled part of SMA connector, $r_1 = 0.635$ mm and $r_2 = 2.25$ mm are the corresponding inner and outer radii, respectively. The dielectric constant of the teflon is approximately $\epsilon_r = 2.2$.

The measurement was performed, as well as simulation, at the frequency range (20 ÷ 2000) MHz with the frequency step 5 MHz. Fig. 35 shows the measured and computed absolute value of an input impedance. As can be seen from the simulation results with and without the model of SMA connector, the influence of the SMA connector cannot be

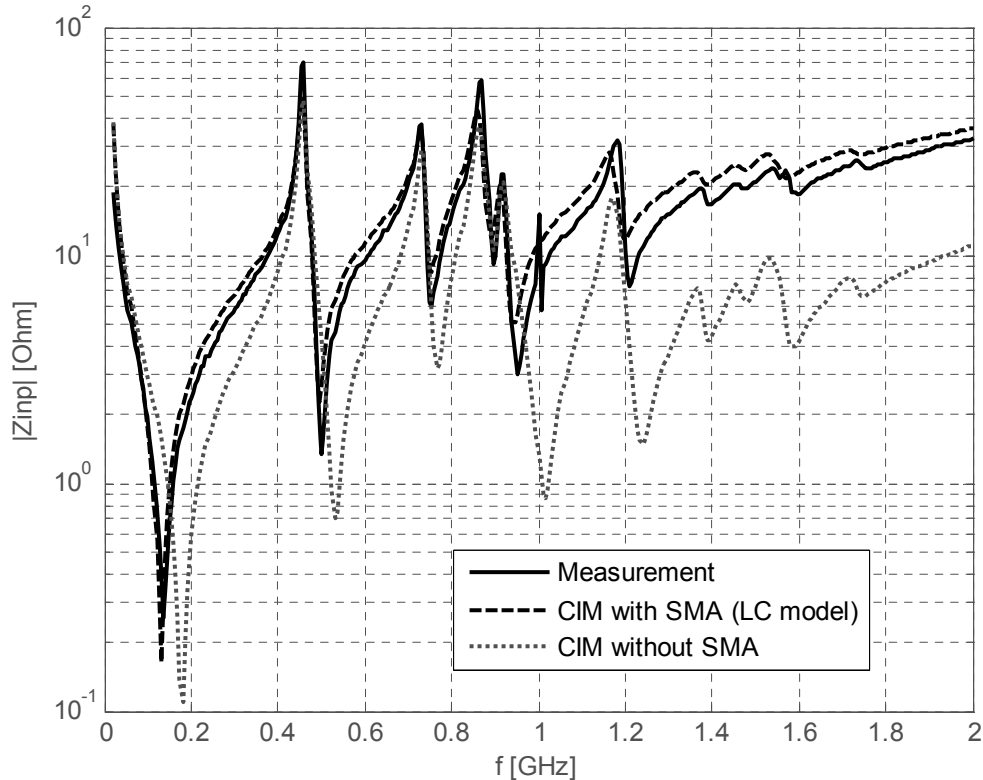


Fig. 35: Absolute value of the input impedance of the tested structure

neglected. The correspondence with the measurement is acceptable. The deviation at higher frequencies is certainly due to the frequency independent modeling of loss mechanism and the

simple modeling of the SMA connector. Additionally, radiation loss is not considered. For circuit-simulation purposes the accuracy is totally sufficient.

The second tested power-bus structure, populated by 13 decoupling capacitors is depicted in Fig. 36. The material was again FR4 with a dielectric constant $\epsilon_r = 4.35$, dissipation factor of $\tan\delta = 0.035$ and thickness of $d = 1.6$ mm. One end of each SMT capacitor was soldered

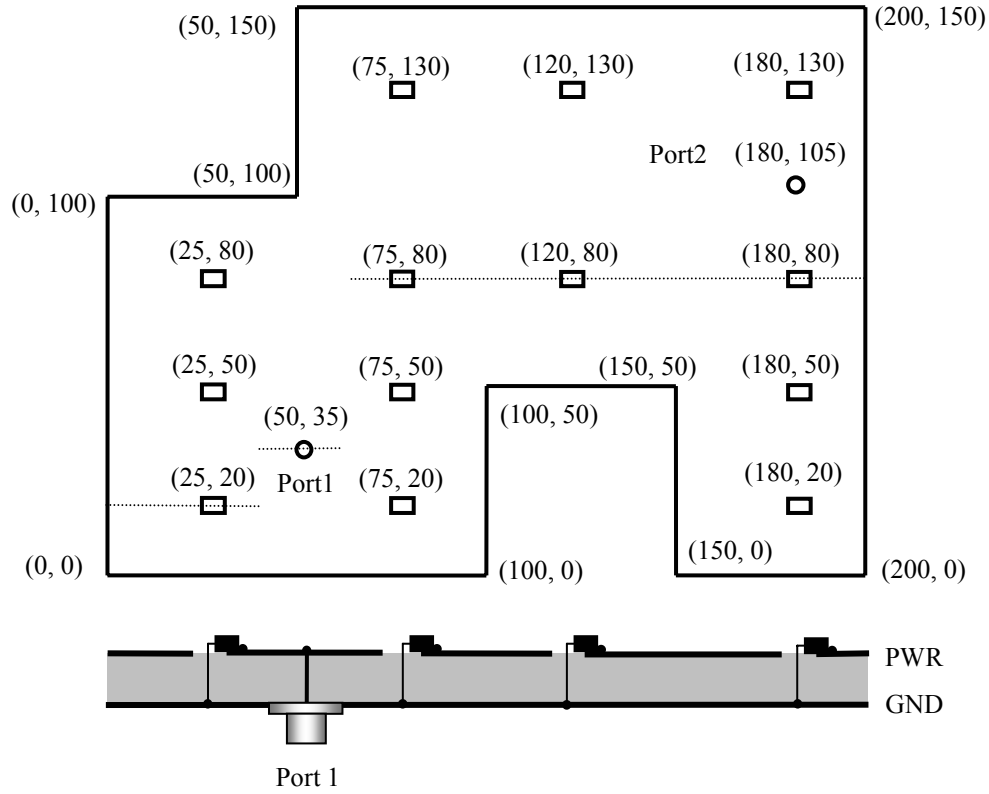


Fig. 36: Power-bus structure including decoupling capacitors
(dimensions in millimeters)

directly to the top power plane and the second end was connected to the ground plane by via with the radius 0.8 mm. Two test ports were constructed using two SMA connectors. The tested power-bus structure was connected by two semi-rigid coaxial cables to the network analyzer and two-port measurement was performed.

Further, the bare multi-port structure was analyzed in Matlab to obtain the voltage-current relations between the ports. All ports modeled in Matlab had the same radius $r = 0.8$ mm. The additive inductance due to the geometry of the port is included in the numerical method. The resulting Z-matrix was converted into the *Touch Stone format* to include the power-bus structure as N-port in ANSOFT Designer. In the last step, the models of the decoupling capacitors and SMA connectors were connected to the pins of the N-port.

Fig. 37 shows the model of a populated power-bus structure with SMA connectors in ANSOFT Designer. All capacitors have the same nominal value $C = 10$ nF. Parasitic inductance ESL and resistance ESR were measured for one capacitor using HIOKI 3535 LCR HiTester with the SMT fixture: ESL = 640 pH and ESR = 120 mΩ. In ANSOFT Designer, the parasitic inductance is included in the resonance frequency of the capacitor model ($f_{res} \approx 62.9$ MHz).

Fig. 38a-c show the $|z_{11}|$ and $|z_{22}|$ parameters for the SMA ports 1 and 2, respectively, and the transfer impedance $|z_{12}|$ between the ports 1 and 2. As can be seen, simulated and measured data are in very good agreement. In conclusion, in Fig. 38d is depicted the transfer impedance $|z_{12}|$ for the bare and decoupled power-bus structure computed in the frequency range (10÷5000) MHz with the step 10 MHz. As can be seen, the decoupling capacitors are effective only at low frequencies.

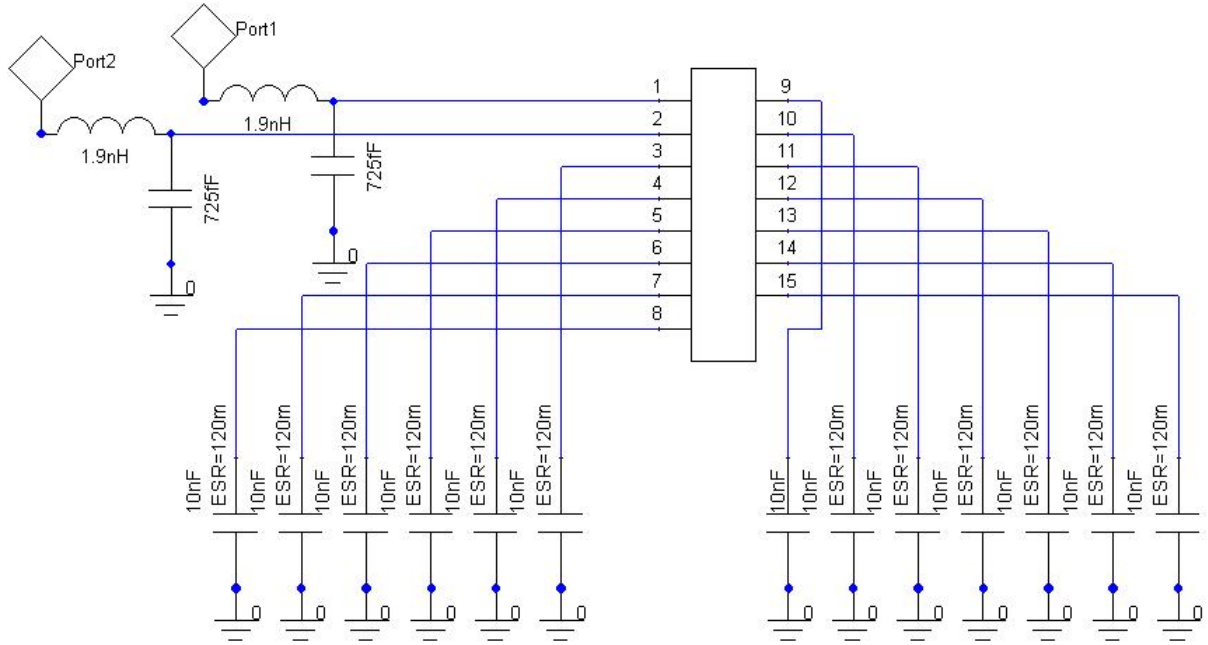


Fig. 37: Model of populated power-bus structure in ANSOFT Designer

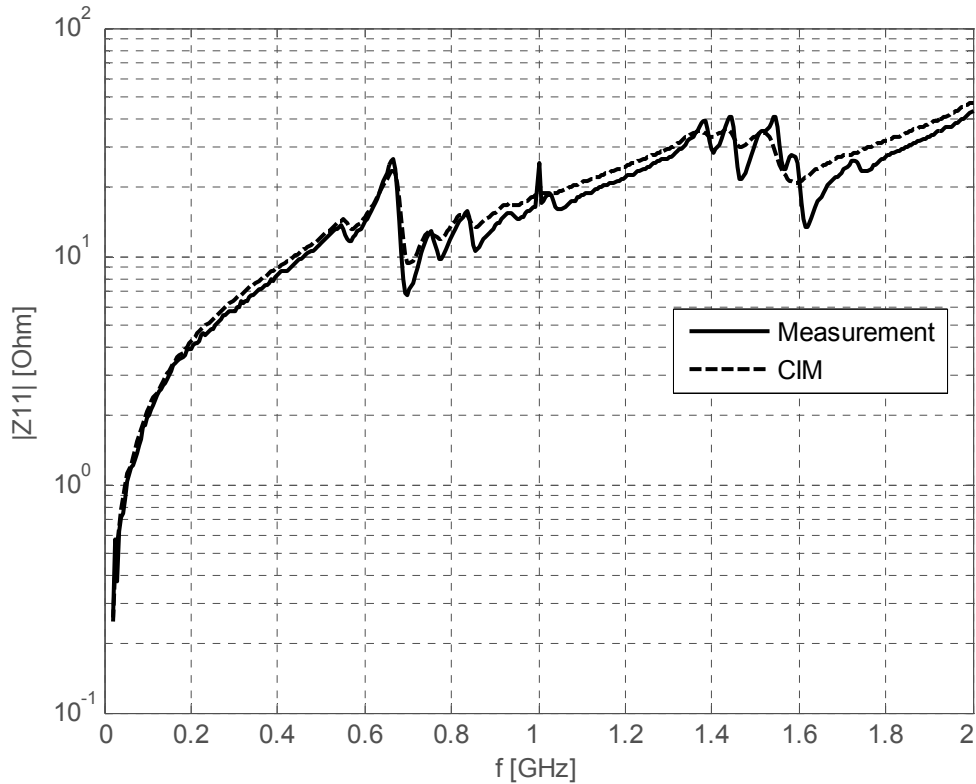


Fig. 38a: Absolute value of z_{11} of the populated power-bus structure

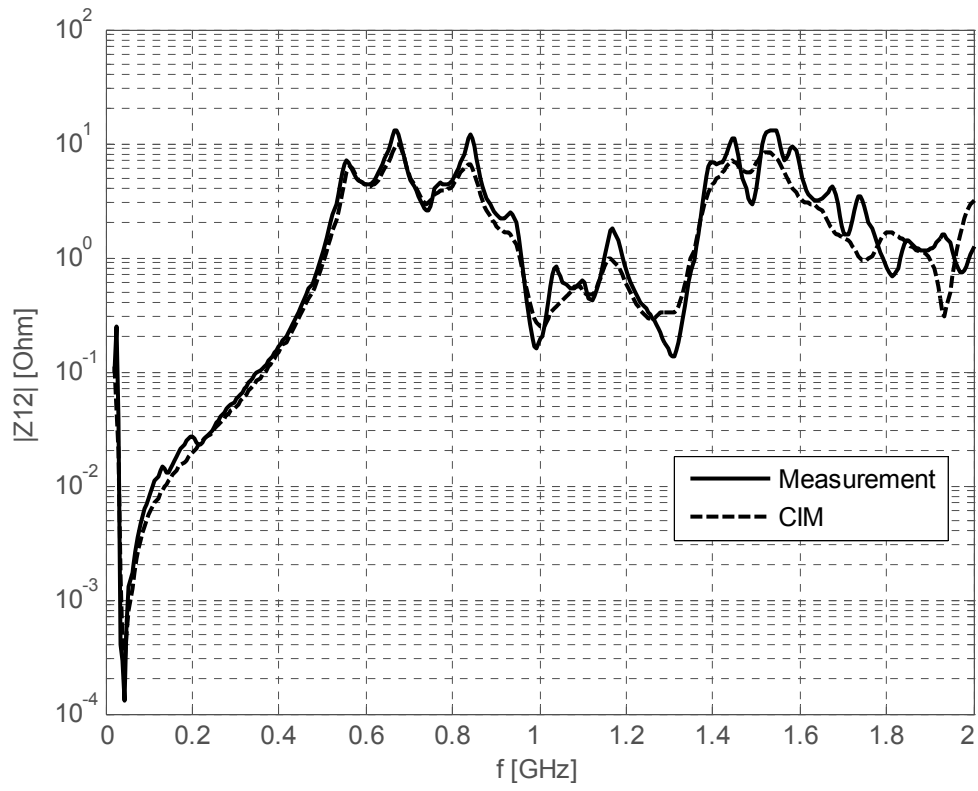


Fig. 38b: Absolute value of z_{12} of the populated power-bus structure

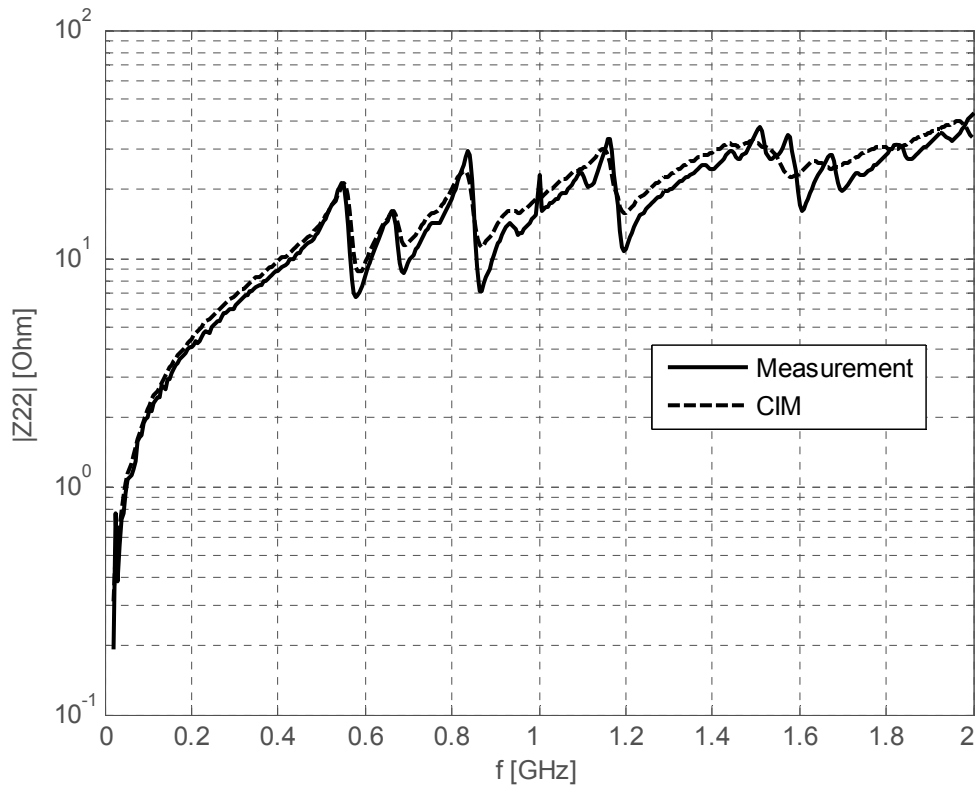


Fig. 38c: Absolute value of z_{22} of the populated power-bus structure

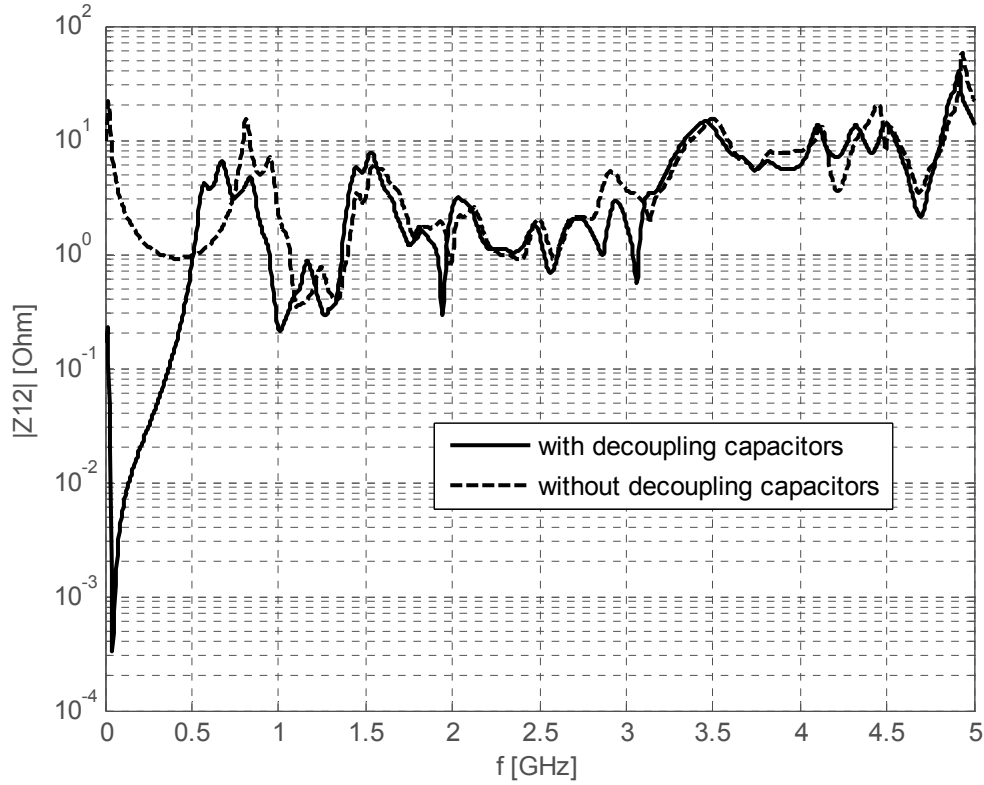


Fig. 38d: *Decoupling effect*

6 Conclusion

A boundary 2D integral equation was used for analysis of the power-bus structures on printed circuit boards. All mathematical details from the general theory were carried out and numerical solution algorithm was implemented in Matlab.

The program is capable to simulate arbitrarily shaped power-bus structures with arbitrary material parameters and number of ports. As output the program provides the voltage/currents relations between the ports in Z-matrix transfer form, voltage distribution between the plates and 3D radiation diagrams. Moreover, the resulting Z-matrix can be converted into the *Touch Stone format*, which can be used to simulate populated power-bus structure in some of the CAD circuit analyzers, e.g. ANSOFT Designer.

In order to validate the Matlab program, the rectangular structure was analyzed first and compared with the analytical solutions. The results of more complex structures were validated using commercial software based on 3D full-wave solver. We have shown that the developed 2D contour integral equation method provides comparable results in a much shorter time than 3D full-wave method of moments as implemented in ANSOFT Designer.

In the last chapter, the numerical approach applied in this thesis was validated by measurements of two power-bus structures. At first, the input impedance of a simple bare rectangular power-bus structure was analyzed and measured. Further the impedance parameters of two-port polygonal power-bus structure populated by a number of decoupling capacitors were simulated and measured. For the SMA connectors, simple LC transmission line model was used. As was found, the calculated results agree quite well with the measurement data over the considered frequency range.

7 References

- [1] LEONE, M. *The Radiation of a Rectangular Power-Bus Structure at Multiple Cavity-Mode Resonances*, IEEE Trans. Electromagn. Compat., vol. 45, no. 3, pp. 486-492, August 2003.
- [2] SOMMERFELD, A. *Partial Differential Equations in Physics*, Academic Press, New York, 1949.
- [3] STRATTON, J. A. *Electromagnetic Theory*, McGraw-Hill, New York, 1941.
- [4] OKOSHI, T. *Planar Circuits for Microwaves and Lightwaves*, Springer-Verlag, 1984, ISBN 3-540-13853-6.
- [5] MORSE, P. M., FESHBACH, H. *Methods of Theoretical Physics*, Part 1, McGraw-Hill, New York, 1953.
- [6] *Touchstone File Format Specification*, EIA/IBIS Open Forum, 2002, [Online], Available: <<http://www.eda.org/pub/ibis/connector/>>
- [7] LIN-KUN, W., CHIH-HSIUNG T., *A theoretical Investigation of the Resonance Damping Performance of Magnetic Material Coating in Power/Ground Plane Structures*, IEEE Trans. Electromagn. Compat., vol. 47, pp. 731-737, November 2005.
- [8] BALANIS, C. A., *Antenna Theory*, New York: Wiley, 1996.
- [9] YE, X., KOLEDINTSEVA, M. Y., LI, M., DREWNIK, J. L. *DC Power-Bus Design Using FDTD Modeling With Dispersive Media and Surface Mount Technology Components*, IEEE Trans. Electromagn. Compat., vol. 43, no. 4, pp. 579-587, November 2001.
- [10] FAN, J., DREWNIK, J. L., SHI H., KNIGHTEN J. L. *DC Power-Bus Modeling and Design With a Mixed-Potential Integral-Equation Formulation and Circuit Extraction*, IEEE Trans. Electromagn. Compat., vol. 43, no. 4, pp. 426-436, November 2001.
- [11] RILEY, K. F., HOBSON, M. P., BENCE, S. J. *Mathematical Methods for Physics and Engineering*, 3rd Edition, Cambridge University Press, 2006.
- [12] FOOKS, E. H., ZAKAREVIČIUS, R. A. *Microwave Engineering Using Microstrip Circuits*, Prentice Hall, 1990.

8 Appendix

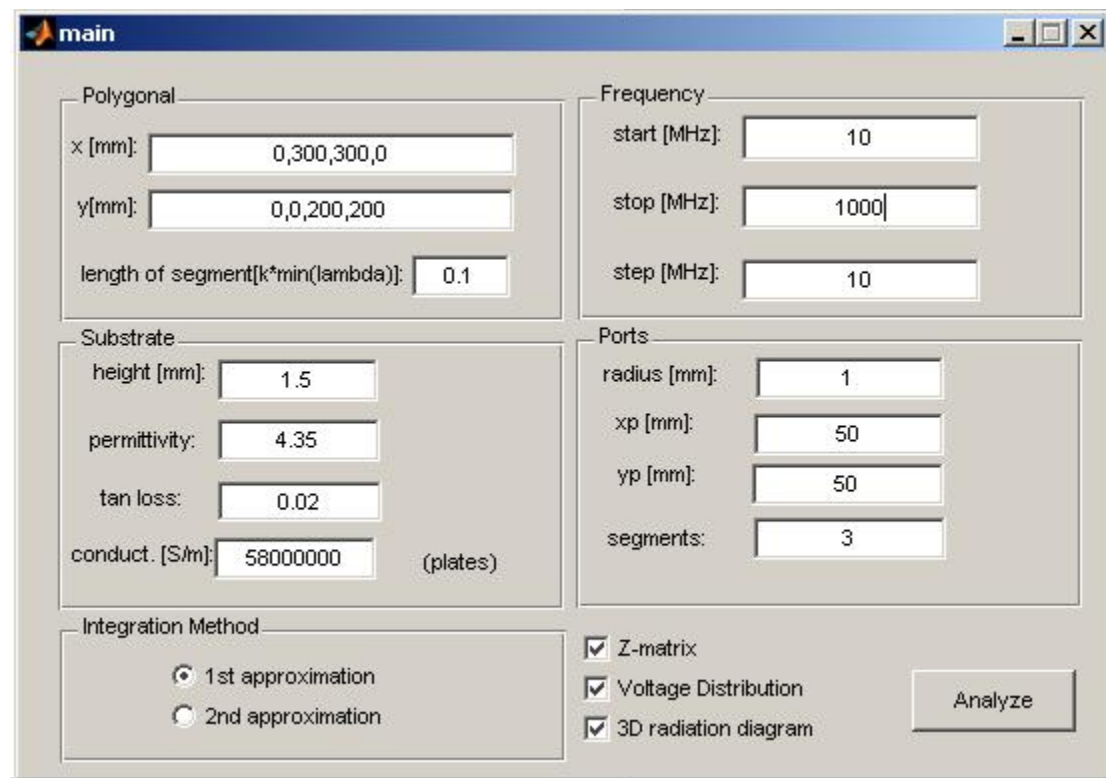


Fig. 39: Graphical user interface of the Matlab program



Fig. 40a: One-port rectangular power-bus structure

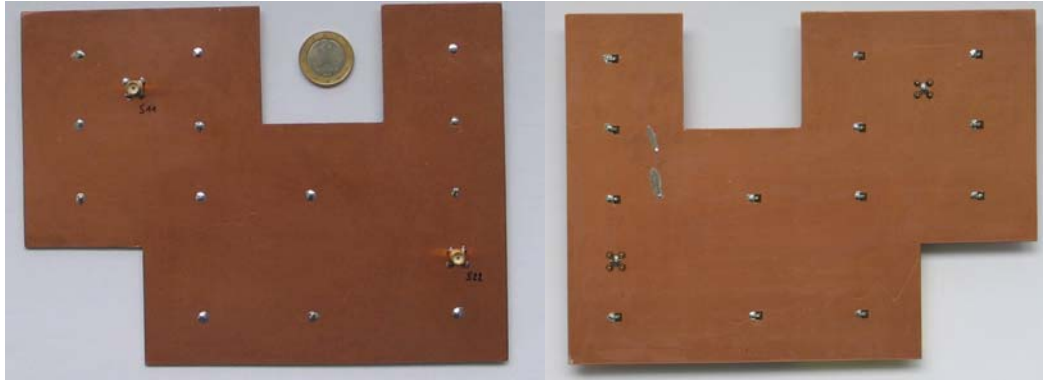


Fig. 40b: *Polygonal two-port power-bus structure loaded with 13 SMT capacitors*